



저작자표시-비영리-변경금지 2.0 대한민국

이용자는 아래의 조건을 따르는 경우에 한하여 자유롭게

- 이 저작물을 복제, 배포, 전송, 전시, 공연 및 방송할 수 있습니다.

다음과 같은 조건을 따라야 합니다:



저작자표시. 귀하는 원저작자를 표시하여야 합니다.



비영리. 귀하는 이 저작물을 영리 목적으로 이용할 수 없습니다.



변경금지. 귀하는 이 저작물을 개작, 변형 또는 가공할 수 없습니다.

- 귀하는, 이 저작물의 재이용이나 배포의 경우, 이 저작물에 적용된 이용허락조건을 명확하게 나타내어야 합니다.
- 저작권자로부터 별도의 허가를 받으면 이러한 조건들은 적용되지 않습니다.

저작권법에 따른 이용자의 권리는 위의 내용에 의하여 영향을 받지 않습니다.

이것은 [이용허락규약\(Legal Code\)](#)을 이해하기 쉽게 요약한 것입니다.

[Disclaimer](#)

공학박사 학위논문

**Dynamic electro-optic modulation
using indium tin oxide- and tungsten
trioxide-based nanostructures**

인듐 주석 산화물과 산화 텅스텐 기반
나노구조체를 이용한 전기광학적 변조

2019 년 8 월

서울대학교 대학원

전기 · 정보공학부

이 요 한

Abstract

Dynamic electro-optic modulation using indium tin oxide- and tungsten trioxide-based nanostructures

Yohan Lee

Department of Electrical and Computer Engineering

College of Engineering

Seoul National University

Over the past decade, there has been an increasing desire to realize active nanophotonic devices based on dynamically reconfigurable nanostructures or metasurfaces. Various mechanisms have been suggested in form of a combination between active materials and well-designed nanostructures at near-infrared (NIR) and visible frequencies, including mechanical actuation, chemical activation, carrier injection, etc. Especially, electrical tuning is one of the most promising techniques due to its distinct advantages such as low power consumption, fast switching speed, and compatibility with existing electronic components.

In this dissertation, general constitutive properties of light such as phase, intensity, and spectrum have been controlled with electric applied bias at NIR and visible regime. Firstly, an electrically tunable amplitude modulator based on indium tin oxide (ITO) as a representative of transparent conducting oxides (TCOs) was proposed to control the optical

signals in NIR range. Beyond the conventional reflective-type metal-insulator-metal (MIM) configuration for gap plasmon resonances, the transmission is modulated using a nanoscale ITO-based capacitor and silicon layer as a high-index waveguide. The proposed modulator is designed to operate with two different types of strong optical modes, hybrid plasmonic waveguide mode and pure waveguide mode. These strongly confined mode provide enhanced light-ITO interaction, which gives rise to detecting the refractive index change by electric field sensitively.

Secondly, a dynamically tunable metasurface designed to implement two functions at one target wavelength was proposed and theoretically investigated. At NIR region, the proposed device is electrically tunable with an ITO-integrated capacitor on a hyperbolic metamaterial substrate, and it can modulate the phase or amplitude of reflected light depending on the condition of incident light. In case of normal incidence, the phase modulation is achieved through the mode called the gap plasmon polariton mode designed to be strongly confined in ITO layer. In addition, to perform the other function on the same structural basis, another type of highly confined modes supported by the hyperbolic metamaterial is utilized. In case of oblique incidence, the amplitude modulation is implemented by coupling between gap plasmon mode and bulk plasmon modes.

Final section of this dissertation contains the contents of electrically tuning the visible light spectrum. Optical properties of WO_3 , a representative of electrochromic material, according to cation intercalation

are analyzed and electrically color-tunable devices based on a WO_3 thin film are demonstrated. Various color generation and high-contrast color tuning is achieved with simple structures which do not require tricky fabrication techniques. Large resonance shift and intensity modification observed by reflective and transmissive type devices are presented and their performance were evaluated.

This dissertation is expected to contribute to the implementation of integrated optical circuits and the commercialization of novel low-powered full-color display in the near future.

Keywords: electrical tuning, indium tin oxide, tungsten trioxide, optical resonance

Student Number: 2014-21682

Contents

Abstract	1
Contents.....	4
List of Tables	6
List of Figures	7
Chapter 1. Introduction	13
1.1 Background.....	13
1.2 Indium tin oxide (ITO) and tungsten trioxide (WO ₃).....	17
1.3 Organization of this dissertation.....	21
Chapter 2. Electrical tuning of transmission in ITO-based metasurface using hybrid plasmonic waveguide	23
2.1 Electronic and optical properties of ITO	23
2.2 Modulator design based on hybrid plasmonic waveguide	27
2.3 Simulation and experimental results.....	35
2.4 Conclusion	45
Chapter 3. Electrically tunable metasurface for integrating phase and amplitude modulation based on hyperbolic metamaterial substrate .	46
3.1 Design and working principle.....	46
3.1.1 Electro-optic mechanism and quantitative analysis	48
3.1.2 Gap plasmon polaritons and bulk plasmon polaritons	50
3.2 Phase modulation with normal incidence.....	55
3.3 Amplitude modulation with oblique incidence.....	58
3.4 Conclusion	62
Chapter 4. Full-color-tunable electrochromic device using WO₃ thin film	63
4.1 Tungsten trioxide as an electrochromic material.....	63
4.2 Reflection-type electrochromic device and color tuning.....	74
4.3 Color-purified transmission-type electrochromic device	80
4.4 Conclusion	85

Chapter 5. Conclusion	87
Bibliography	90
Appendix	97
초 록	98

List of Tables

Table 1.1 Various mechanisms for dynamically tuning optical signals	16
Table 4.1 Sputtering conditions for WO ₃ thin film deposition	64

List of Figures

- Figure 1.1** (a) Photographic image of electronic circuit with ITO electrode. (b) Dielectric permittivity of ITO fitted by Drude model as a function of wavelength and carrier density.19
- Figure 1.2** Electrochromic phenomenon using WO_3 on ITO-coated glass. The color changes from transparent to deep blue.20
- Figure 2.1** (a) Spatial distribution of carrier density and (b) the real value part of permittivity of ITO at wavelength of 1400 nm as a function of position from the Al_2O_3 / ITO interface for different voltages.24
- Figure 2.2** The measured (a) real and imaginary (b) part of complex refractive indices of deposited ITO as a function of wavelength for different sputtering conditions. Experimental results are shown as solid lines, while dashed line indicates calculated results fitted by Drude model.26
- Figure 2.3** (a) The schematic of the proposed modulator. (b) Working principle of electrically driven transmission modulator. The inset depicts a nanoscale MOS capacitor accumulates charges at the Al_2O_3 / ITO interface via applied voltages. (c) Scanning electron microscope images of fabricated patterns.28
- Figure 2.4** (a) The effective index and (b) mode character of hybrid mode as a function of the thickness of Si layer for different the thickness of oxide.31
- Figure 2.5** The calculated transmittance as a function of the incident wavelength and the Si thickness. With the condition of a 320-nm-thick-Si layer, two resonant wavelengths are described as P_1 and P_232

Figure 2.6 The square of norm of electric field distribution at each resonance (a) P ₁ and (b) P ₂ in Figure 2.5.....	33
Figure 2.7 Dispersion diagram for the proposed structure and Si-free structure.	34
Figure 2.8 Calculated transmittance of the proposed modulator as a function of the incident wavelength for different applied voltages.	35
Figure 2.9 Schematic of the electrically tunable modulator where voltage is applied between the nano-patterns and ITO layer. (b) Photographic image of fabricated sample. (c) Fabrication process for the proposed structure.	37
Figure 2.10 Fabrication process of nanoslit array patterns with E-beam lithography.	38
Figure 2.11 Bode plot of the impedance of proposed device. Magnitude expressed in logarithmic scale and phase angle of the impedance are simultaneously plotted.	39
Figure 2.12 Experimental setup for measuring the transmission spectra of the modulator.	40
Figure 2.13 Photographic image of experimental setup.	41
Figure 2.14 Measured transmission spectrum (Blue) with no applied bias and the trend line based on measured data (Red).	42
Figure 2.15 (a) Calculated transmission spectra for different incident angles. (b) The summation of transmission spectra for different incident angles. The range of incident angle is from 0 to 20 degrees.....	43
Figure 2.16 Measured transmittance spectra for different applied bias.	44

Figure 3.1 (a) Schematic of unit cell of the proposed device. The Au nanograting is placed on the Au-HfO₂-ITO capacitor, and the HMM that consists of the 3 sets of Au-HfO₂ multilayer is under the capacitor as a substrate. Unit cell dimensions are chosen as follows: width of grating $w = 230$ nm, and periodicity of unit cell $p = 530$ nm. Each thickness of grating, ITO, Au, and HfO₂ is $t_g = 50$ nm, $t_s = 20$ nm, $t_m = 20$ nm, $t_o = 10$ nm. (b) Real and imaginary parts of effective permittivity of Au-HfO₂ HMM calculated using effective medium theory. The dielectric permittivity tensor component in the parallel direction and the normal direction are depicted as solid and dashed lines, respectively.48

Figure 3.2 (a) Spatial distribution of carrier density and (b) the real value part of permittivity of ITO at wavelength of 1450 nm as a function of position from HfO₂ / ITO interface for different voltages. The charge accumulation region dependent on the voltage is divided into 13 layers in order to simulate the real condition accurately as much as possible (red rectangles). Gray area highlights the spatial region where the real value of permittivity acquires values between -1 and 1 representing the ENZ region..50

Figure 3.3 Three kinds of high-k modes. The spatial distribution of y-component of magnetic field at gap plasmon (left panel), bulk plasmon (center panel), and surface plasmon (right panel) resonance.52

Figure 3.4 Cyclic voltammograms for different (a) the film thickness and

(b) scan rate.54

Figure 3.5 For normal incidence, (a) Color map of the reflectance versus wavelength and applied voltages. (b) Calculated complex reflectance as a function of applied voltages for the wavelength of 1450 nm. Applied voltage increases along the clockwise direction. (c) Simulated phase shift and intensity as a function of applied voltages at target wavelength of 1450 nm. (d) The spatial distribution of y -component of magnetic field of reflected light when the applied voltage is -2 V (Left panel) and 3 V (Right panel).57

Figure 3.6 Dispersion relation of the proposed structure. Color map of the simulated reflectance versus wavevector and wavelength for the proposed structure (left panel) and the structure without HMM in the proposed one (right panel). The various types of resonance are named (Inset: structure diagrams).59

Figure 3.7 For oblique incidence of 60° , (a) color map of the reflectance versus wavelength and applied voltages. (b) Calculated complex reflectance as a function of applied voltages for target wavelength of 1450 nm. Applied voltage increases along the clockwise direction. (c) Simulated phase shift and intensity as a function of applied voltages at operating wavelength of 1450 nm. (d) The intensity of magnetic field of reflected light when the applied voltage is -2 V (Left panel) and 3 V (Right panel).61

Figure 4.1 Cyclic voltammograms in 100 mM LiClO_4 electrolyte (acetonitrile) for different (a) the film thickness and (b) scan rate.....66

Figure 4.2 Steady state potential and diffusion coefficient as a function of x

in Li_xWO_3 via galvanostatic intermittent titration technique (GITT).....	68
Figure 4.3 X-ray photoelectron spectra of (left) as-prepared WO_3 film in the region of W (upper-left) and O (bottom-left). X-ray photoelectron spectra of WO_3 after Li intercalation are presented on the right column in the region of W (upper-right) and O (bottom-right).	69
Figure 4.4 X-ray diffraction spectrum of WO_3 thin film deposited on highly doped Si wafer.	70
Figure 4.5 Scanning electron microscopy image of (a) as-sputtered WO_3 film and (b) WO_3 after Li intercalation/de-intercalation cycle.....	71
Figure 4.6 The optical properties of WO_3 thin film as a function of the amount of Li^+ injection. (a) Refractive index and (b) absorption coefficient are measured with a range of wavelength between 350 nm to 1650 nm...	73
Figure 4.7 The schematic illustration of reflection-type color generation and tuning.	75
Figure 4.8 (a) Reflectance of WO_3 thin film on Si as a function of the incident wavelength and the thickness of WO_3 . (b) Photographic image of fabricated red, green, and blue samples with target thickness.....	76
Figure 4.9 Calculated (top) and experimental (bottom) spectra of reflected light. Color variation corresponding to each same colored spectrum from state 1 through 4 to 6 (inset).	77
Figure 4.10 The reversibility and stability test of the WO_3 -based structure. The spectrum change of a 235-nm-thick WO_3 on Si of state (a) $x = 0$ and (b) $x = 0.38$ for different Li^+ intercalation cycles.	78

Figure 4.11 The reflected spectra of a 165-nm-thick WO_3 on Si of state 6 for different time conditions immersed in electrolyte.79

Figure 4.12 The schematic illustration of transmissive type electrochromic device. The working principle is described.81

Figure 4.13 (a) Transmittance of $\text{Ag}/\text{WO}_3/\text{Ag}$ on quartz substrate as a function of the incident wavelength and the thickness of WO_3 . (b) Photographic image of fabricated red, green, and blue samples with target thickness.82

Figure 4.14 Spectra tuning of transmitted light for R, G, B. Light on/off corresponding to each same colored spectrum from state 1 through 4 to 6 (inset).84

Chapter 1. Introduction

1.1 Background

Nanophotonics, the study on the interaction of nanometer scale object with light, has exhibited a great potential to complement or replace the existing optical devices [1]. Unlike quantum mechanics, the Maxwell equations have a scalable property regardless of the length of the wavelength, thus nanophotonics shares much of the research in different wavelength such as microwave, THz, and infrared. Since the discovery of surface plasmon polaritons (SPPs), the quasi-particles generated at the surface of conductive materials by a collective oscillation of photons and electrons [2], the problem that normal optical components generally cannot focus light to deep subwavelength scales has been solved [3]. After that, nanophotonics has exhibited a tremendous potentials for current technologies aiming to replace the existing photonics, and it has been developed through various research themes such as near-field microscopes [4,5], nano-lasers [6,7], and metamaterials [8,9] with the mature of nano-fabrication and manipulation techniques of nano-objects in recent 20 years.

In particular, metamaterials and metasurfaces are rising fields

nowadays in nanophotonics due to their anomalous and largely tunable properties of light scattering in ultracompact volume [10–12]. Metamaterials are artificially engineered three-dimensional periodic structures that enable to control electromagnetic wave in the extraordinary manner [11,13]. Also, metasurfaces are two-dimensional subwavelength scale arrangement of meta-atoms composed of one or more nanostructures with noble metals or high index dielectrics. Desired effective local optical responses such as amplitude, phase, and polarization are tailored by metamaterials and metasurfaces. Ultracompact optical devices based on exotic functionalities have been replacing conventional bulk ones such as lens [14,15], polarizers [16,17], and waveplates [18], and various applications have been intensively demonstrated including hologram [19,20], refractive index sensing [21–23], anomalous beam refraction [24], and vortex generation [25]. However, the range of applications of metamaterials- or metasurfaces-based devices are restricted since the functionalities are determined once they are fabricated.

In recent days, substantial efforts have been focused on reconfigurable and switchable metasurfaces with active materials driven by thermal effect [26], electrical tuning [27,28], chemical activation [29–33], and mechanical reconfiguration [34] as shown in Table 1.1. With the enhanced freedom and multifunctionalities, active metasurfaces have shown great promises for novel application including sensors, data storage, imaging, and encryption at NIR and visible frequencies. Among these various approaches, electrical tuning with electro-optic or electro-chemical materials is one of most

promising method due to its distinct merits including lower power dissipation, high modulation speed, and compatibility with semiconductor photonic devices. Active materials such as graphene [35,36], highly doped semiconductors [37], phase change materials (PCMs) [26,38–40], transition metal dichalcogenides [41], and transparent conducting oxides (TCOs) [27,28,42–44] have been thoroughly studied and used to modulate light by combining with optical devices composed of nanostructures.

In particular, dynamic control of visible light is one of the ultimate goals in nanophotonics for displaying applications. After color generation by plasmonic nanostructures or metasurfaces with extremely high resolution was achieved [45–48], significant efforts have been directed toward the spectrum tuning in the visible with various approaches such as liquid crystal-enabled modulation, reversible electrodeposition [49,50], electrochromism [51,52], chemical catalysis [53], and Purcell effect [54]. However, all of these techniques still cannot reach the requirements for ideal display applications due to the difficulties in improving color purity, extending color gamut, and fabricating large area from inevitably complicated configuration. Therefore, a strategic approach is needed for better performance and device structure which requires simple and economic fabrication process, as well as fundamental research on switchable materials and their mechanisms.

	Mechanisms			
	Phase change by thermal energy	Mechanical reconfiguration	Chemical reaction	Electrical tuning
Materials	VO ₂ , GST	-	Mg, Pd	Graphene, TCOs, Highly doped semiconductors
Pros	- Large modulation depth	- Low power consumption - Connectivity with other mechanisms	- Extremely large modulation depth	- Fast switching - Low power consumption - Compatibility with existing electronic components
Cons	- Lower speed - High power consumption	- Lower speed	- Reversibility - Very low speed	- Small change in the effective optical constants

Table 1.1. Various mechanisms for dynamically tuning optical signals

1.2 Indium tin oxide (ITO) and tungsten trioxide (WO₃)

As a composition of indium, tin, and oxygen in varying proportions, indium tin oxide (ITO) is one of the most widely used TCOs due to its two distinct properties: optical transparency and electrical conductivity (Figure 1.1a). Because ITO is a kind of heavily doped *n*-type semiconductor with a large bandgap of around 4 eV, its extinction coefficient in the visible range is near zero and it is mostly transparent. On the other hand, it is opaque in the NIR and infrared (IR), because of free carrier absorption that an infrared photon can excite an electron from near the bottom of the conduction band to higher within the conduction band. It is well known that a compromise must be made between transparency and conductivity since increasing the thickness and increasing the concentration of charge carriers increases the ITO's conductivity, but decreases its transparency. The conductivity of ITO can be controlled by the oxygen content during deposition.

In nanophotonics, ITO has been intensively studied due to their electrical depletion or accumulation phenomenon with metal-oxide-semiconductor (MOS) configuration. This nanoscale capacitor is capable of controlling the amount of carriers formed at the ITO / insulator interface by applied electric field [55]. It means that the refractive index of local region can be adjusted by external electric stimulus. Such index change, however, occurs only very near the interface, and it is difficult to achieve sufficient

large optical modulation. To overcome short interaction length / time between light and active region, most reported studies have been designed based on gap plasmon resonance that occurs in metal-insulator-metal (MIM) waveguide [27,28,42,43,55,56]. This design can give extremely high modal confinement to enhance light-matter interaction and lead to a larger modulation depth.

Furthermore, to enhance interaction between ITO and electromagnetic wave, the configurations have been suggested based on epsilon-near-zero (ENZ) condition. As the requirements imposed by the boundary conditions that are provided by Maxwell's equations are considered, the continuity of the normal components of the electric displacement field leads to strong discontinuities in the normal electric field because of the near zero permittivity in the ENZ materials [57]. ITO has been usually used by fitting to Drude model due to its relatively large conductivity, therefore the dispersion relation shows that the real part of dielectric permittivity becomes zero, indicating the existence of ENZ point (Figure 1.1b). In case of ITO, this type of ENZ behavior can be found over a wide frequency range from the NIR to mid-IR because the carrier density has a variety of values in several oxygen contents.

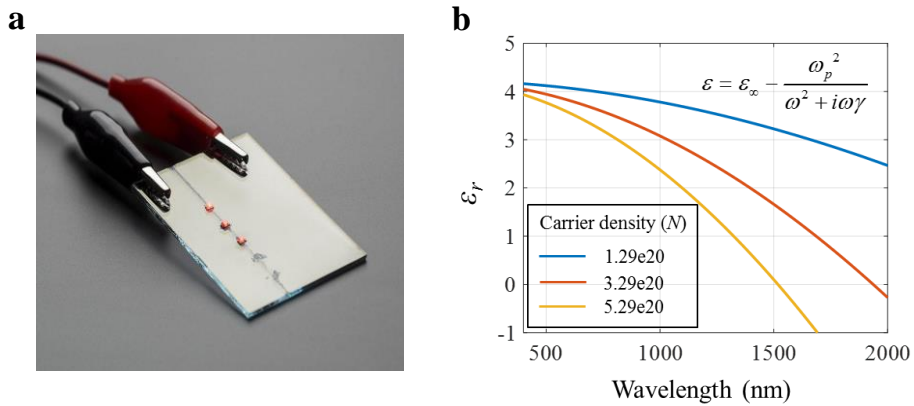


Figure 1.1. (a) Photographic image of electronic circuit with ITO electrode. (b) Dielectric permittivity of ITO fitted by Drude model as a function of wavelength and carrier density.

Also, tungsten trioxide (WO_3) is used in this dissertation to control optical spectrum in the visible beyond the NIR regime. As a chemical compound containing the transition metal tungsten and oxygen, WO_3 is frequently used for photocatalysts [58], gas sensors [59], Li-ion battery [60], corrosion protection layers, and high- k dielectrics in capacitors. It is also used as a pigment in paints due to its rich yellow color. On the other hand, WO_3 has been the most extensively studied material for electrochromism [61], the phenomenon where the color of a material changes by applying a voltage. It has been employed in the production of smart windows, or electrochromic windows. These windows are electrically switchable glass that change light transmission properties with an applied voltage. In this thesis, research on WO_3 material as an electrochromic device was

introduced.

When WO_3 , which is transparent as a thin film, incorporates various cations such as sodium, potassium, and proton, it can be reversibly transformed to a material with radically different properties. This is due to the structural change of WO_3 , which greatly affects the optical properties of the material. In bleached state, the extinction coefficient of WO_3 is usually zero, thus it is mostly transparent. However, the extinction coefficient increases after cation intercalation within WO_3 , and the longer wavelength of light is more absorbed. Therefore, the color of WO_3 changes from transparent to deep blue (Figure 1.2). However, there are two main issues on WO_3 as an electrochromic material: monochromic color tuning and high power consumption from micro-thickness scale.

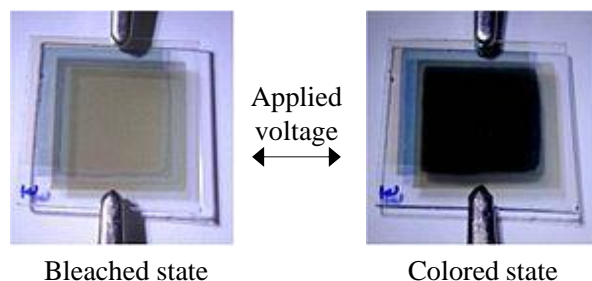


Figure 1.2. Electrochromic phenomenon using WO_3 on ITO-coated glass.

The color changes from transparent to deep blue.

1.3 Organization of this dissertation

This dissertation deals with electrically tunable optical devices based on two semiconductor oxides, ITO and WO₃.

In Chapter 2, electrical tuning of transmission in ITO-based metasurface using hybrid plasmonic waveguide is proposed. In section 2.1, electronic and optical properties of ITO thin film are analyzed. In section 2.2, device design and its working principle based on the contents of section 2.1 is explained. The details in device fabrication are shown and the performance of the proposed device is numerically and experimentally demonstrated in section 2.3. Finally, the conclusion and brief discussion are presented in section 2.4.

In Chapter 3, at the fixed target wavelength, an electro-optical device that can simultaneously control the amplitude and phase of the reflected light is proposed. This device has added its functionalities based on the work introduced in Chapter 2. The design and working principle of the proposed device is explained in section 3.1. The section 3.2 accounts for the operation of the proposed device as a phase modulator with normal incidence. In addition, amplitude modulation with oblique incidence is explained in section 3.3. The conclusion and brief discussion are presented in section 3.4.

In Chapter 4, tungsten trioxide as an electrochromic material is

introduced in section 4.1. In section 4.2, the deposition method and optical properties of tungsten oxide thin film are explained. In reflection type, various color generation and tuning with applied voltages are demonstrated in section 4.3. In addition, a transmission-type device with better color purity than the reflection-type is proposed in section 4.4. The conclusion and brief discussion for applications to practical display systems are explained.

In Chapter 5, a summary of this dissertation is presented, and perspectives of the proposed devices are discussed.

Chapter 2. Electrical tuning of transmission in ITO-based metasurface using hybrid plasmonic waveguide

2.1 Electronic and optical properties of ITO

In order to understand the amount of accumulated charges and the refractive index change according to the applied voltages, a one-dimensional MOS capacitor model consisting of Au, Al₂O₃, and ITO was analyzed based on the Poisson equation.

$$\frac{d^2\psi}{dx^2} = -\frac{q}{\epsilon_{semi}} \left[N_a \left(e^{-q\psi/kT} - 1 \right) - \frac{n_i^2}{N_a} \left(e^{q\psi/kT} - 1 \right) \right]. \quad (1)$$

It was assumed that the thickness and the DC dielectric constant of Al₂O₃ as a gate insulator was 10 nm and 9.1, the work-function of Au as a gate electrode was 5.1 eV, and the carrier density of ITO was $3 \times 10^{20} \text{ cm}^{-3}$. Spatial distribution of the carrier density and the real part of permittivity of ITO are respectively calculated for different applied voltages as a function of distance from Al₂O₃ / ITO interface. It can be seen that the larger voltage is applied, the more accumulated charges which cause optical loss increases (Figure 2.1a). Also, the real part of dielectric permittivity of ITO changes from positive to negative (Figure 2.1b). This means that the proposed device

can operate on the condition of epsilon-near-zero (ENZ) region, namely, the real part of permittivity is between -1 and 1, which offers a large electric field.

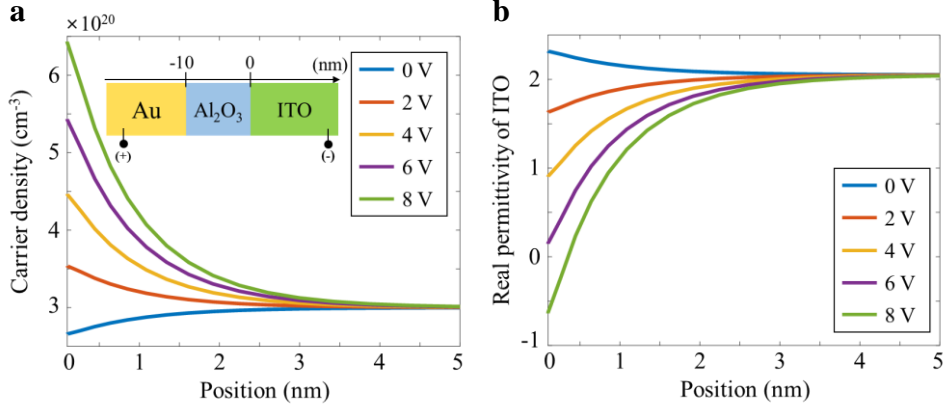


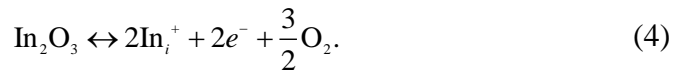
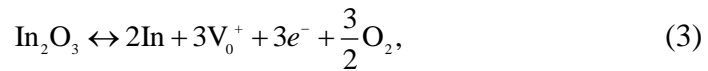
Figure 2.1. (a) Spatial distribution of carrier density and (b) the real value part of permittivity of ITO at wavelength of 1400 nm as a function of position from the Al₂O₃ / ITO interface for different voltages.

Prior to designing the modulator, the complex permittivity of ITO should be precisely analyzed. It is well known that the dielectric permittivity of ITO can be analyzed by Drude model due to its high conductivity, which is given by

$$\epsilon_{\text{ITO}} = \epsilon_{\infty} - \frac{\omega_p^2}{\omega^2 + i\Gamma\omega} = \epsilon_{\infty} - \frac{Ne}{m^* \epsilon_0} \frac{1}{\omega^2 + i\Gamma\omega}. \quad (2)$$

where ω_p is the plasma frequency, ϵ_{∞} is dielectric permittivity at infinite frequency, N is carrier density, e is the electron charge, m^* is electron effective mass, ϵ_0 is the dielectric permittivity of vacuum, and Γ is damping

constant. It is worth noting that the permittivity of ITO can be controlled by adjusting N in Equation 2, and control of N is the fundamental principle of electro-optic modulator based on ITO layers. N of ITO is adjustable by changing the ratio of Ar / O₂ during sputtering since In₂O₃ has point defects that consist of oxygen vacancies or the interstitial indium atoms, giving rise to free electrons in reduction environment. The chemical equations about In₂O₃ during annealing process are indicated by Equations 3 and 4.



In Equations 3 and 4, V_0^+ and In_i^+ are oxygen vacancies and interstitial indium atoms, and e^- is carrier electron. If the rate of O₂ is higher during annealing process, the reverse reactions in Equations 2 and 3 occur more actively, thus the density of free electron (N) will decrease. To confirm this, the samples were prepared with 50 nm-thick ITO on a Si wafer. In the chamber of sputter, there are two valves for Ar and O₂ to control the flow rate. The flow rate of Ar was fixed as 25 sccm and varied for O₂ from 0.1 to 0.3 gradually. Then, ellipsometry was used with the prepared samples. Figures 2.2a and 2.2b show the measured refractive index of ITO and the absorption coefficient as a function of O₂ flow rate, respectively. As expected, the refractive index increases as the flow rate of O₂ increases because the decrease of N also reduces the value of the plasma frequency in Drude equation (Equation 2). Among several conditions, 0.2 of the O₂ flow

rate (scarlet curve) was chosen, and fitted the measured data with Drude model. By fitting with measured results, the values of Drude parameters were determined. The carrier concentration of ITO incorporated by the proposed modulator was $N = 3 \times 10^{20} \text{ cm}^{-3}$, dielectric permittivity at infinite frequency (ϵ_{∞}) was 4.4, and electron effective mass (m^*) was $0.22 \times m_e$. Literature value for the damping constant Γ was used as $1.8 \times 10^{14} \text{ radHz}$. It is seen that the choice of values provides an excellent agreement between the calculated and measured values.

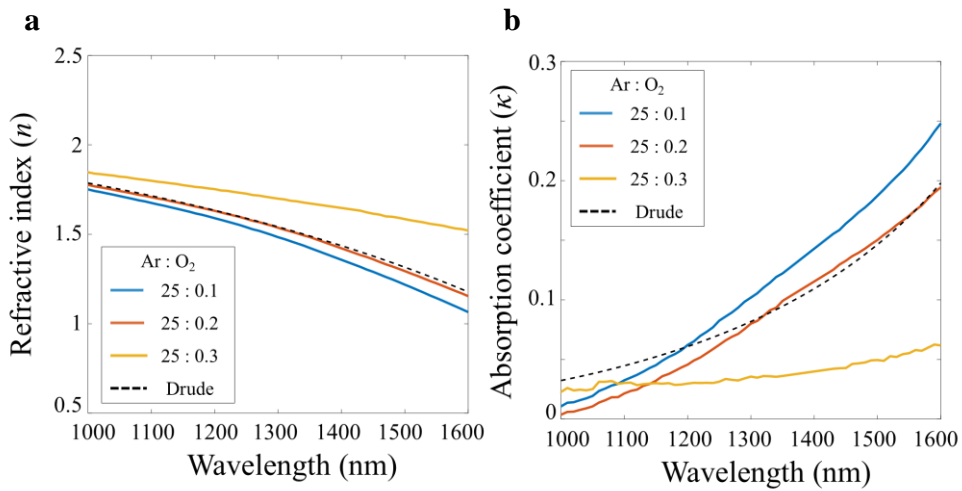


Figure 2.2. The measured (a) real and imaginary (b) part of complex refractive indices of deposited ITO as a function of wavelength for different sputtering conditions. Experimental results are shown as solid lines, while dashed line indicates calculated results fitted by Drude model.

2.2 Modulator design based on hybrid plasmonic waveguide

A one-dimensional array of $w = 100$ nm wide and $t_m = 40$ nm thick Au slit patterns is arranged with the periodicity $p = 900$ nm. The nano-patterns are on top of an Al_2O_3 / ITO / amorphous silicon (Si) stack of which thicknesses are respectively $t_o = 10$ nm, $t_s = 20$ nm, and $t_{\text{Si}} = 320$ nm (Figure 2.3a). The device incorporates a nanoscale MOS capacitor, which is a well-known configuration to generate charge accumulation or depletion phenomenon at the semiconductor / oxide interface by applying electric field. Spatial distribution of carrier concentration near the ITO / Al_2O_3 interface varies depending on applied bias. The real part of dielectric permittivity of charge accumulated- or depleted-region decreases and the imaginary part increases as the applied voltage increases, because the material properties of the layer become more metallic as more negative charges are accumulated. The proposed modulator, under normal illumination with a transverse magnetic (TM) polarization, shows high transmission with no applied voltage. In contrast, when the voltage is applied to the device, charge-accumulated-region forms at the ITO / Al_2O_3 interface and the loss from accumulated charges hinders optical transmission (Figure 2.3b). Scanning electron microscope (SEM) images of fabricated nanoslit is provided in Figure 2.3c. The nanoslit patterns bound in a group are connected external gold pads as an electrode.

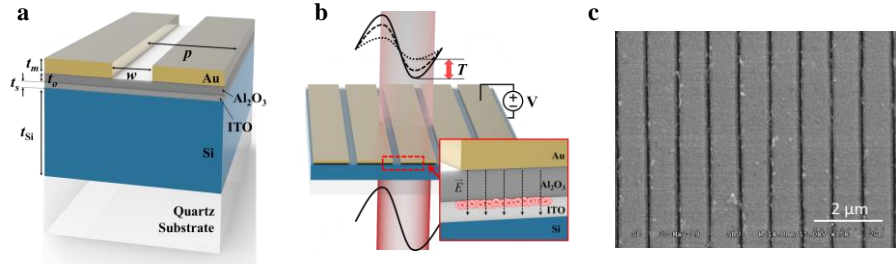


Figure 2.3. (a) The schematic of the proposed modulator. (b) Working principle of electrically driven transmission modulator. The inset depicts a nanoscale MOS capacitor accumulates charges at the Al_2O_3 / ITO interface via applied voltages. (c) Scanning electron microscope images of fabricated patterns.

Carrier-induced index change in this nanoscale MOS configuration, however, is confined only in an ultrathin layer as shown in Figure 2.1a. In case of the proposed device with carrier concentration $3 \times 10^{20} \text{ cm}^{-3}$, the thickness of the modulated region is around 1 nm. This implies that extreme field confinement in this region is needed to achieve tunable optical response. For strong light concentration in ITO and enhanced interaction, in the proposed device, a Si waveguide separated from the Au nanoslit array by Al_2O_3 and ITO gap is incorporated with the nanoscale MOS configuration. This combination between periodic Au nanoslits and a high effective index waveguide can support the guided mode resonance. This resonance has been intensively studied as a spectral filter due to its extremely high transmittance or reflectance with ultra-narrow bandwidth. This mode can be excited when

the first-order diffracted waves by nanoslit array satisfy the inequality with the assumption of normal incidence.

$$\max [n_{\text{air}}, n_{\text{SiO}_2}] \leq \frac{\lambda_0}{p} < n_{\text{WG}}. \quad (5)$$

In Equation 5, n_{air} , n_{SiO_2} , and n_{WG} indicate the refractive index of air, SiO₂, and waveguide composed of Al₂O₃, ITO, and Si. λ_0 is the incident wavelength. Equation 5 means that the first-order diffracted waves are trapped in the waveguide by total reflection.

In addition to guided mode resonance, the proposed configuration can support different type of strong resonance, that is, the hybrid plasmonic waveguide resonance. This hybrid mode made by the coupling between SPP mode excited at the metal surface and waveguide mode by a dielectric layer has extremely high effective index and can be strongly confined across the gap like an optical capacitance [62]. This is because a polarization charge induced by the dielectric discontinuity at the Si / ITO interface interacts with the SPP of the Au / Al₂O₃ and enhances a normal component of electric field. To understand the coupling effect between two optical modes, the hybrid mode is expressed as a superposition of the two basic modes, the Si waveguide mode and the SPP mode, using a coupled mode theory:

$$\psi_{\text{Hyb}}(t_o, t_{\text{Si}}) = a(t_o, t_{\text{Si}})\psi_{\text{wg}}(t_{\text{Si}}) + b(t_o, t_{\text{Si}})\psi_{\text{SPP}}, \quad (6)$$

where $a(t_o, t_{\text{Si}})$ and $b(t_o, t_{\text{Si}})$ correspond to each amplitude of the waveguide $\psi_{\text{wg}}(t_{\text{Si}}) = \{1 \ 0\}^T$ and SPP modes $\psi_{\text{SPP}} = \{0 \ 1\}^T$ basis modes as a multivariable function of the thickness of Al₂O₃ (t_o) and Si layer (t_{Si}). The

modes of the coupled system are characterized by the system of equations

$$\begin{pmatrix} n_{\text{wg}}(t_{\text{Si}}) & V(t_o, t_{\text{Si}}) \\ V(t_o, t_{\text{Si}}) & n_{\text{SPP}} \end{pmatrix} \begin{pmatrix} a(t_o, t_{\text{Si}}) \\ \sqrt{1-|a(t_o, t_{\text{Si}})|^2} \end{pmatrix} = n(t_o, t_{\text{Si}}) \begin{pmatrix} a(t_o, t_{\text{Si}}) \\ \sqrt{1-|a(t_o, t_{\text{Si}})|^2} \end{pmatrix}, \quad (7)$$

where $V(t_o, t_{\text{Si}})$ is the coupling strength between two modes and mode amplitude normalization implies $b(t_o, t_{\text{Si}}) = \sqrt{1-|a(t_o, t_{\text{Si}})|^2}$. The mode reflects the quadratic nature of the characteristic equation of the coupled mode theory, for which the solutions are $n(t_o, t_{\text{Si}}) = \bar{n}(t_{\text{Si}}) \pm \Delta(t_o, t_{\text{Si}})$, where $\bar{n}(t_{\text{Si}}) = [n_{\text{wg}}(t_{\text{Si}}) + n_{\text{SPP}}] / 2$, and $\Delta(t_o, t_{\text{Si}})^2 = (n_{\text{wg}} - n_{\text{SPP}})^2 / 4 + V(t_o, t_{\text{Si}})^2$. In this case, the mode amplitude $|a(t_o, t_{\text{Si}})|^2$ provides a measure of the character of the hybrid mode given by

$$|a(t_o, t_{\text{Si}})|^2 = \frac{V(t_o, t_{\text{Si}})^2}{(n(t_o, t_{\text{Si}}) - n_{\text{wg}}(t_{\text{Si}}))^2 + V(t_o, t_{\text{Si}})^2}. \quad (8)$$

Equation 8 can be rewritten in the form presented using the solution for $n(t_o, t_{\text{Si}})$ and then equating $n_{\text{hyb}}(t_o, t_{\text{Si}}) = n(t_o, t_{\text{Si}})$ with the effective mode index of hybrid (n_{hyb}), waveguide (n_{wg}), and SPP (n_{SPP}):

$$|a(t_o, t_{\text{Si}})|^2 = \frac{n_{\text{hyb}}(t_o, t_{\text{Si}}) - n_{\text{SPP}}}{[n_{\text{hyb}}(t_o, t_{\text{Si}}) - n_{\text{wg}}(t_{\text{Si}})] + [n_{\text{hyb}}(t_o, t_{\text{Si}}) - n_{\text{SPP}}]}. \quad (9)$$

Figure 2.4 shows the effective indices of hybrid mode for the different thickness of Al_2O_3 and Si layer compared with the n_{wg} (magenta line) and n_{SPP} (black line). The effect of mode coupling can be seen that the hybrid mode index is higher than that of two pure wave and SPP modes. Also, the

n_{hyb} is reduced as the t_o increases because the mode coupling is weakened due to the separation of the metal and waveguide.

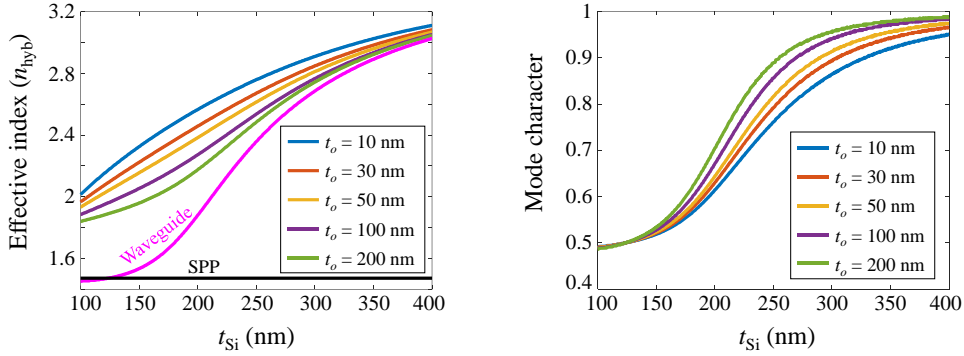


Figure 2.4. (a) The effective index and (b) mode character of hybrid mode as a function of the thickness of Si layer for different the thickness of oxide.

To confirm two strong resonances abovementioned in the proposed structure, the transmittance as a function of the incident wavelength and the Si thickness is numerically simulated (Figure 2.5). As expected, it can be seen that the incident light can transmit only in the two resonance regions and is blocked in the other regions. With the condition of $t_{\text{Si}} = 320$ nm, each resonant wavelength is 1329 nm (P_1) and 1410 nm (P_2), respectively. It can be seen that the guided mode resonance displays significantly higher quality factor than the hybrid plasmonic waveguide mode. This facilitates effective electromagnetic field concentration in active region in ITO.

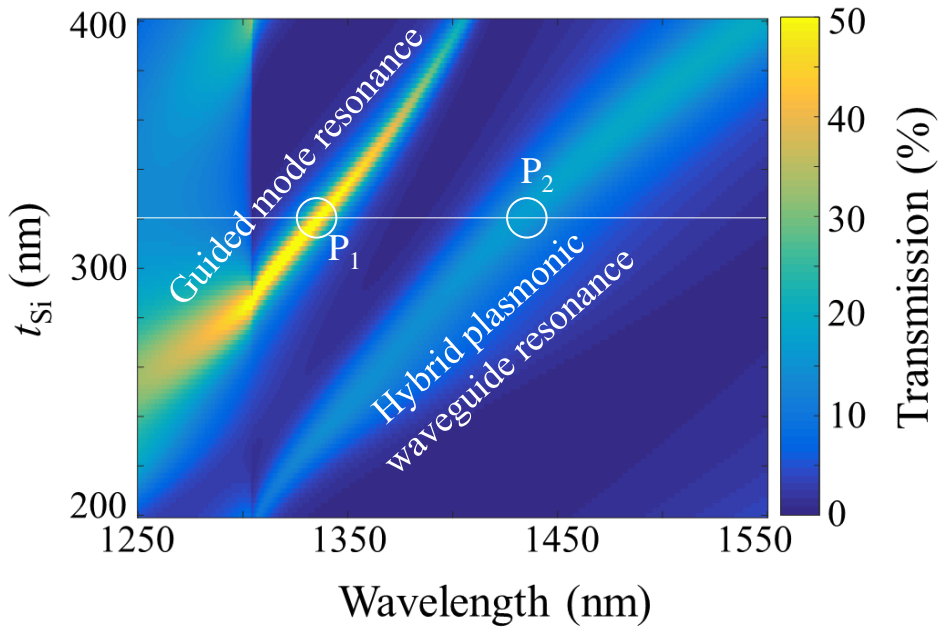


Figure 2.5. The calculated transmittance as a function of the incident wavelength and the Si thickness. With the condition of a 320-nm-thick-Si layer, two resonant wavelengths are described as P_1 and P_2 .

To identify the type of each resonance, the electromagnetic field distribution is described (Figure 2.6). The square of the norm of electric field distributions shows clearly the field confinement in the waveguide. At P_1 , the standing wave is formed inside the waveguide. In case of P_2 , the plasmonic resonance is shown under the Au nanoslit and interferes with waveguide mode. In addition, the square of the norm of the electric field indicates the field confinement in the structure. Hybrid mode (P_2) is strongly confined in ITO and Al_2O_3 layer than the pure waveguide mode (P_1) so that the light-active material interaction is more enhanced.

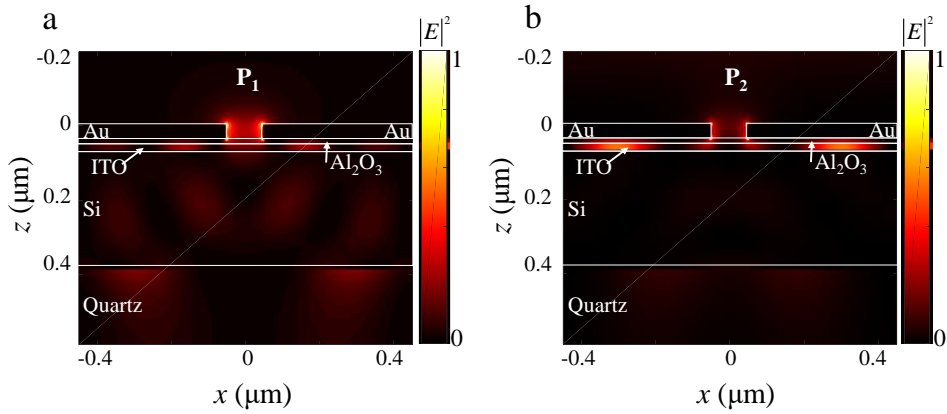


Figure 2.6. The square of norm of electric field distribution at each resonance (a) P_1 and (b) P_2 in Figure 2.5.

To understand the role of Si waveguide more specific, dispersion relation is calculated for two cases: the nano-patterns on Si waveguide (the proposed structure) and the nano-patterns without Si waveguide (Figure 2.7). Blue curve has a greater inclination to the right than red one owing to high refractive index of Si. Meanwhile, dashed curves in Figure 2.7 shows the changed dispersion when the real value of refractive index of Al_2O_3 varies by 0.2 (n decreases from 1.746 to 1.546). Dispersion diagram indicates that the proposed structure requires greater energy compensation compared to Si-free case in frequency region of our interest. In other words, the proposed modulator works as highly sensitive refractive index sensor within the frequency regime we are interested because Si can help more sufficient interaction between light and extremely ultrathin accumulation layer in active material and achieving higher modulation depth.

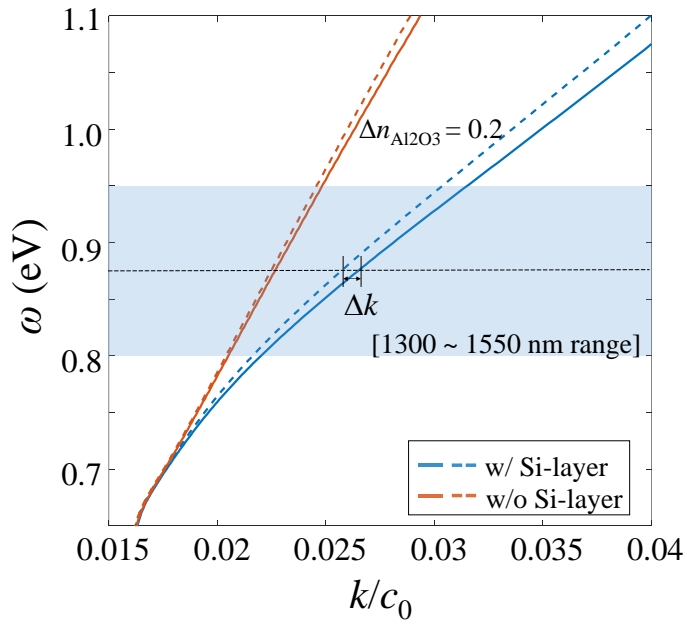


Figure 2.7. Dispersion diagram for the proposed structure and Si-free structure.

2.3 Simulation and experimental results

The transmission spectra for different applied voltages under normal incidence of TM wave on the proposed device are calculated in Figure 2.8. The resonance based on guided mode shows high quality factor but not much modulation depth ΔR . As shown in previous section 2.2, a guided mode is formed in entire waveguide at resonance, thus the electromagnetic energy cannot be confined on the active region sufficiently. On the other hand, hybrid plasmonic waveguide resonance shows lower transmission than guided mode resonance, but superior relative change of reflectance $\Delta R/R$. This is because the gap between an Au nanoslit array and Si waveguide acts as an optical capacitor.

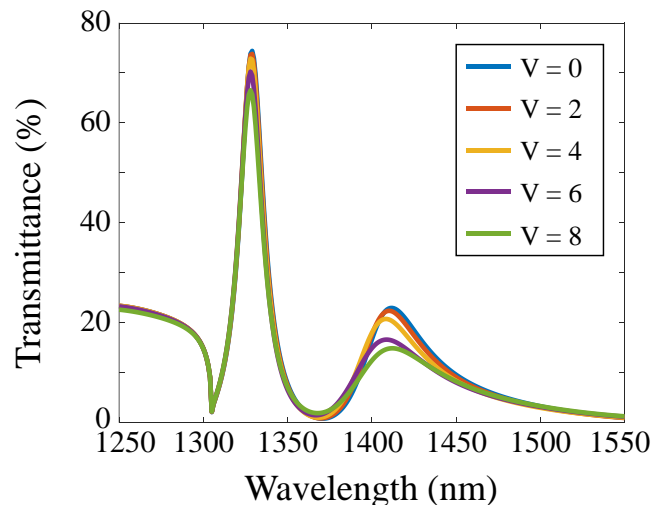


Figure 2.8. Calculated transmittance of the proposed modulator as a function of the incident wavelength for different applied voltages.

The proposed modulator is fabricated via multiple thin-film deposition, standard photo and E-beam lithography. First of all, a 320-nm-thick-Si layer is deposited by plasma-enhanced chemical vapor deposition (PECVD) on quartz glass substrate (P5000, AMAT). Then, the sample is coated with hexamethyldisilazane (HMDS) at a speed of 4000 rpm for 30 seconds and baked at a temperature of 120 degrees Celcius for 3 minutes. This process helps for better adhesion between Si layer and photo resist. Positive photo resist (TDMR AR87) is spin-coated at a speed of 4500 rpm for 40 seconds and soft-baked at a temperature of 88 degrees Celcius for 90 seconds. With chrome mask, the hard contact exposure is carried out by aligner (MA-6 III, Karl-suss) with the 25mW power for 5 seconds. After exposure, the development of the resist was performed by AZ300 MIF for 60 seconds. The sample was rinsed with deionized water and hard-baked at a temperature of 113 degrees Celcius for 90 seconds.

Then, a 20-nm-thick ITO layer is deposited by DC magnetron sputtering in Ar / O₂ plasma (CS-200, ULVAC). Target source is indium oxide (In₂O₃) and tin dioxide (SnO₂) in a 90 to 10 weight percent ratio. Sputtering was carried out at chamber pressure of 6.5 mTorr at a sputtering power of 2 kW, by changing the ratio of Ar / O₂ to obtain different optical properties of the ITO. Here, it is hard to identify the alignment pattern filled with ITO, thus the alignment pattern is gold-plated. Next, 10 nm of Al₂O₃ was deposited by atomic layered deposition (ALD) method. For contact

pads, abovementioned photolithography with same conditions is carried out once more with another patterned chrome mask. Finally, the nanoslit array is patterned by lift-off process on the stack.

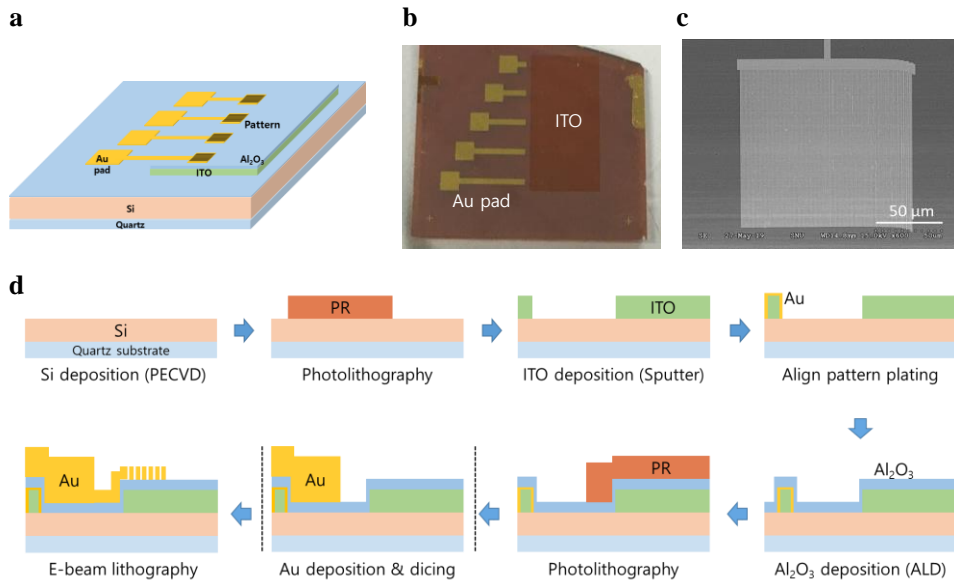


Figure 2.9. (a) Schematic of the electrically tunable modulator where voltage is applied between the nano-patterns and ITO layer. (b) Photographic image of fabricated sample. (c) Fabrication process for the proposed structure.

Schematic of the modulator is depicted in Figure 2.9a where voltage is applied between the nano-patterns via gold contact pads and ITO layer. Photographic image of the device is provided in Figure 2.9b. The inset of Figure 2.9b shows a close-up look of the fabricated device. Figure 2.9c shows the fabrication process of our gate-tunable amplitude modulator.

The details of nano-patterning with E-beam lithography are as follows.

Figure 2.10 shows a schematic of the e-beam lithography process. The sample was coated by bilayer E-beam resist to facilitate lift-off process. Positive resist PMMA was used for both layers. Bottom PMMA (MicroChem Corp., PMMA 950K A4) was spin-coated at a speed of 3000 rpm for 40 seconds and baked at a temperature of 180 degrees Celcius for 60 seconds. Successively, top PMMA (MicroChem Corp., PMMA 950K A2) was once more spin-coated at a speed of 2000 rpm for 40 seconds and baked under the same conditions abovementioned. The patterning is carried out by E-beam lithography (JEOL, JBX-6300FS) at an acceleration voltage of 100 keV with 1 nA current. After exposure process, the development of the resists was performed by manually agitating the sample in MIBK / IPA (1:3) for about 90 seconds. Then, a 40 nm of Au layer was deposited by thermal evaporator with the 0.2 nm s⁻¹ of deposition rate. At last, the sample was immersed in acetone for 24 hours followed by sonication for 10 seconds to get rid of residuals except Au patterns.

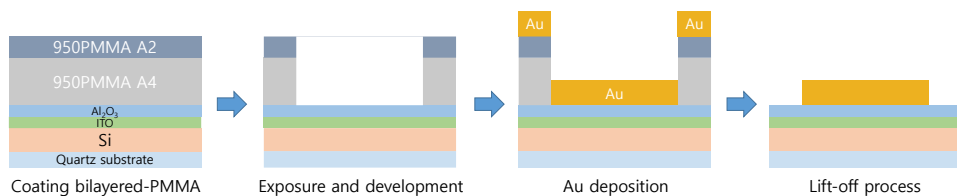


Figure 2.10. Fabrication process of nanoslit array patterns with E-beam lithography.

To verify that the fabricated device works well electrically, impedance

spectroscopy was conducted by applying 10 mV AC input over a frequency range from 100 kHz to 10 Hz with a potentiostat (Reference 600, Gamry Instrument, US). The impedance spectrum was analyzed by Zview2 (Scribner Associates, US) software. DC bias was applied and the current was recorded by Compactstat (Ivium Technologies, The Netherlands). At low frequencies, the impedance is resistance-like. Measured resistance is approximately 2 M Ω at DC environment. This means that the leaky current is about sub-micro ampere level. Over the 100 Hz, capacitive properties begin to occur, and the angle of the impedance becomes nearly 90 degrees (Figure 2.11).

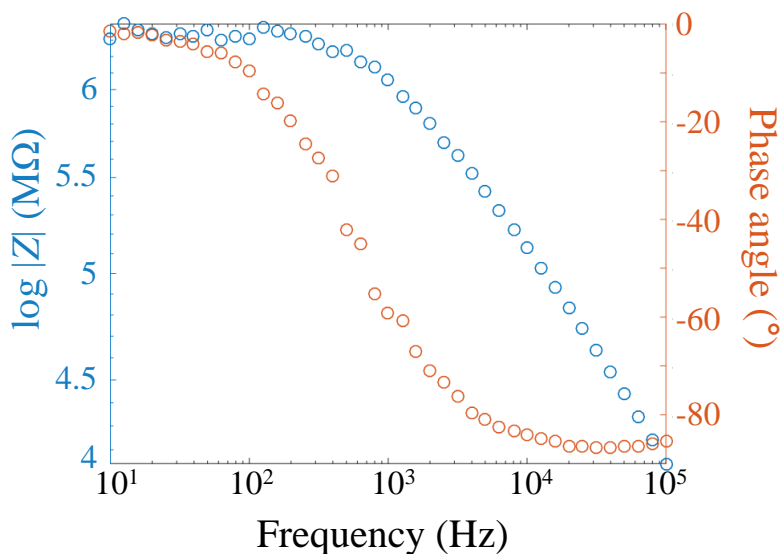


Figure 2.11. Bode plot of the impedance of proposed device. Magnitude expressed in logarithmic scale and phase angle of the impedance are simultaneously plotted.

The transmission through the metasurface is detected by microscopic setup as shown in Figure 2.12. Broadband supercontinuum source is directed through linear polarizer to be TM polarization against nanogratings. Then, a lens is placed on the sample to focus the polarized light. The position of focused light is adjusted to the center of sample by using portable microscope. The transmitted light is collimated and coupled into optical spectrum analyzer through optical fiber. The measured transmission intensity is normalized relative to intensity in the area transmitted through just quartz glass substrate.

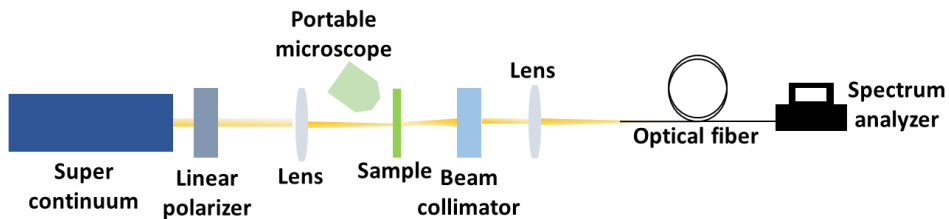


Figure 2.12. Experimental setup for measuring the transmission spectra of the modulator

Figure 2.13 shows the photographic image of experimental setup. One can visually distinguish the portable microscope, polarizer, collimator, lens, and optical fiber. Sample and fiber are on the XYZ stages to move their positions.

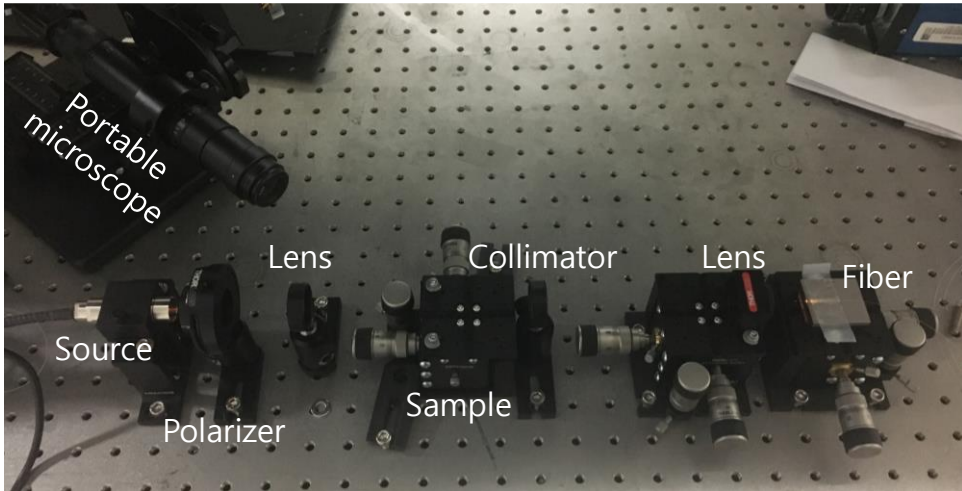


Figure 2.13. Photographic image of experimental setup.

The transmission spectrum is measured as shown in Figure 2.14. Two resonances at around 1320 nm and 1420 nm are experimentally observed, which correspond to GMR and hybrid plasmonic waveguide resonance. It can be seen that there is a lot of noise in the signal due to the high power of supercontinuum source (Blue spectrum). Therefore, a trend line is drawn based on measured spectrum (Red spectrum). There is slight difference between the simulation and experimental results (Figure 2.8 and 2.14). This is because the input beam is focused by lens, and various angular components other than the normal component are generated in this process. In numerical simulation, it is assumed that only normal component of input wave is incident to the sample. To confirm this error, additional simulation is conducted for different incident angles (Figure 2.15).

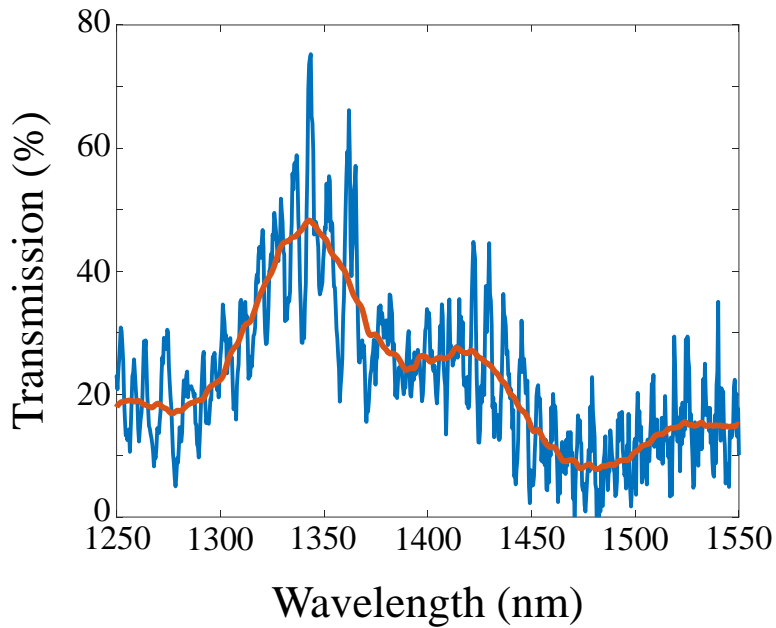


Figure 2.14. Measured transmission spectrum (Blue) with no applied bias and the trend line based on measured data (Red).

As shown in Figure 2.15a, it can be seen that GMR is more vulnerable than hybrid plasmonic waveguide resonance. Although the angle of incidence has changed slightly, GMR breaks and shifts to shorter wavelength. On the other hand, hybrid plasmonic waveguide resonance shows only reduction of transmission and does not move until the incident angle is about 10 degrees. Figure 2.15b shows the Gaussian summation of input beam for various angular components. This result shows good agreement between simulation and experimental results.

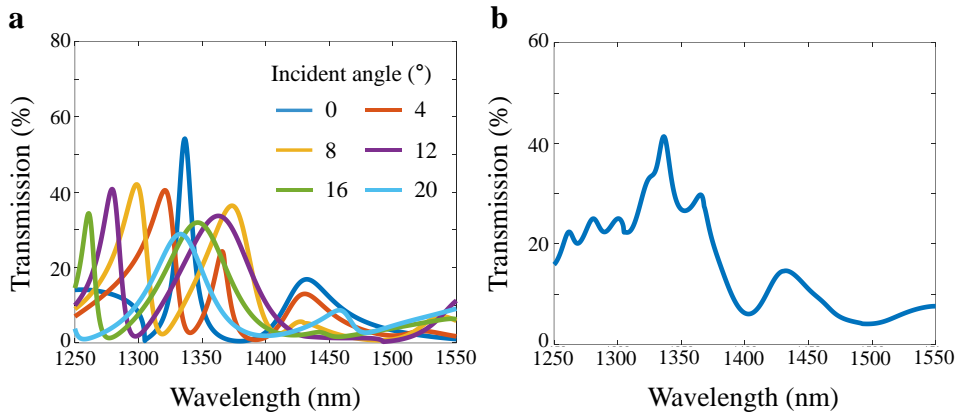


Figure 2.15. (a) Calculated transmission spectra for different incident angles. (b) The summation of transmission spectra for different incident angles. The range of incident angle is from 0 to 20 degrees.

The transmission spectra are measured for different applied bias as shown in Figure 2.16. The transmission change (normalized to the transmission without applied voltage, $\Delta T / T_0 = [T(V) - T(0)] / T(0)$) is high as 21.24 % for operating wavelength under an applied voltage of 6 V. The sample is electrically break-down when a voltage of 6 V or more was applied, and no longer showed a change in transmission depending on the applied voltage.

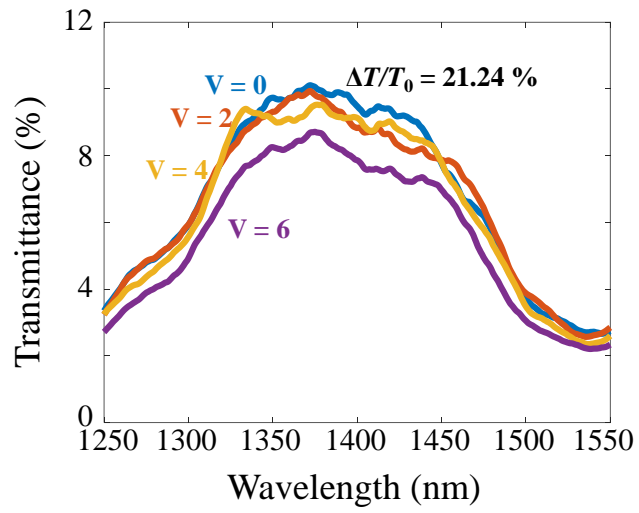


Figure 2.16. Measured transmittance spectra for different applied bias.

2.4 Conclusion

In conclusion, an electrically tunable transmission modulator that works well even with fast AC input based on ITO, a representative of TCOs, is proposed. The proposed device is designed to operate with two different types of strong optical modes, hybrid plasmonic waveguide mode and pure waveguide mode, which have extremely high modal index. The guided mode resonance displays significantly higher quality factor that facilitates effective electromagnetic field concentration in an active region of ITO. In addition, the coupled hybrid mode between the waveguide and plasmonic modes enables energy storage across the gap between the waveguide and metal. This strongly confined mode offers enhanced light-ITO interaction, which gives rise to detecting the refractive index change sensitively. The megahertz modulator demonstrates a transmission modulation of 30 % and operates at each resonant wavelength.

Chapter 3. Electrically tunable metasurface for integrating phase and amplitude modulation based on hyperbolic metamaterial substrate

3.1 Design and working principle

Schematic illustration of the unit cell of proposed device is depicted in Figure 3.1a. The device consists of a nanoscale MOS capacitor on the HMM substrate and a two-dimensional metallic nanogratings placed on the top. These three components of the proposed device are respectively utilized to demonstrate electrically-driven modulator, to support strongly confined modes [63], and to couple the incident light matching the momentum conditions inside the structure. The HMM is constructed by alternatively stacking 3 sets of metal (Au) and dielectric (HfO₂) layers. Since the metal-dielectric multilayer is stacked along the z -direction, the HMM exhibits anisotropic characteristics, which means the uniaxial dielectric tensor components are different from each other ($\varepsilon_{\parallel} = \varepsilon_x = \varepsilon_y$ and $\varepsilon_{\perp} = \varepsilon_z$). Figure 3.1b shows the calculated relative permittivity tensor of HMM using the effective medium theory [64]. This is possible since the thickness of Au and

HfO₂ layer is sufficiently thin to be respectively 20 nm and 10 nm compared to the wavelength of incidence. It is confirmed that the HMM shows a hyperbolic dispersion at interesting wavelengths, where $\epsilon_{\parallel} < 0$ and $\epsilon_{\perp} > 0$. The detailed physical mechanisms of each component and its working principles are explained as follows.

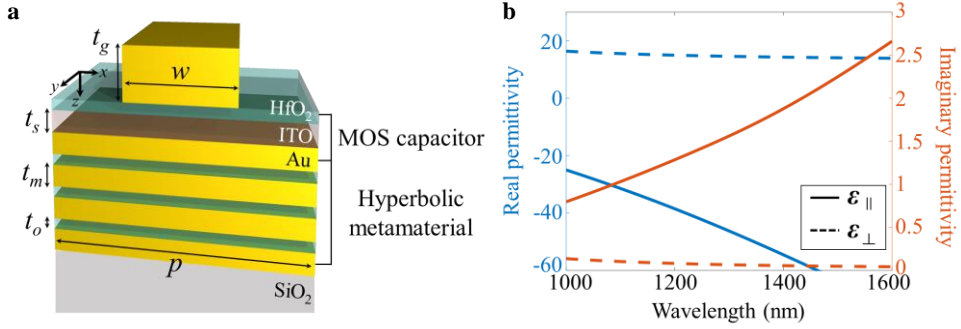


Figure 3.1. (a) Schematic of unit cell of the proposed device. The Au nanograting is placed on the Au-HfO₂-ITO capacitor, and the HMM that consists of the 3 sets of Au-HfO₂ multilayer is under the capacitor as a substrate. Unit cell dimensions are chosen as follows: width of grating $w = 230$ nm, and periodicity of unit cell $p = 530$ nm. Each thickness of grating, ITO, Au, and HfO₂ is $t_g = 50$ nm, $t_s = 20$ nm, $t_m = 20$ nm, $t_o = 10$ nm, respectively. (b) Real and imaginary parts of effective permittivity of Au-HfO₂ HMM calculated using effective medium theory. The dielectric permittivity tensor component in the parallel direction and the normal direction are depicted as solid and dashed lines, respectively.

3.1.1 Electro-optic mechanism and quantitative analysis

In the proposed device, the MOS capacitor consists of gold (Au), hafnium oxide (HfO₂), and ITO (Inset of Figure 3.1a). As a key component of active control, the MOS capacitor accumulates or depletes charges in active layer according to the direction of applied electric field. Details on

MOS capacitor are explained in section 2.1. It was assumed that the relative DC permittivity of HfO₂ is 25 at the static condition. Figure 3.2a shows the calculated carrier densities at the HfO₂ / ITO interface under various applied voltages. Especially, the thickness of HfO₂ is carefully designed to prevent dielectric breakdown. The range of voltage application is set from -2 to 3 V since the breakdown field of HfO₂ is known to be approximately 3.1 MVcm⁻¹. Electron depletion at the interface occurs when the zero voltage is applied. This phenomenon is due to charge redistribution by electron diffusion under equilibrium conditions. An accumulation layer is formed in ITO at the HfO₂ / ITO interface when the voltage application is larger than 1 V, and more charges accumulate with higher voltages. Importantly, substantial changes are concentrated within around 4 nm under various bias, whereas the carrier concentration over this active region maintains the background carrier density value regardless of an external electric field. In particular, it reaches the ENZ region at an applied bias of approximately 1.9 V, and the sign of the real value of permittivity changes from positive to negative under higher bias of 1.9 V (Figure 3.2b). It means that the region where charges accumulate becomes more metallic and lossy. In our simulations, the 5 nm region is divided into 13 layers to reflect the actual situation more accurately.

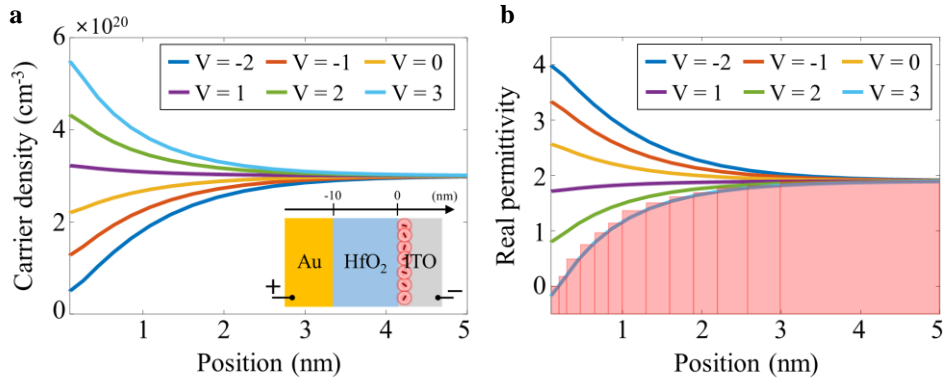


Figure 3.2. (a) Spatial distribution of carrier density and (b) the real value part of permittivity of ITO at wavelength of 1450 nm as a function of position from HfO₂ / ITO interface for different voltages. The charge accumulation region dependent on the voltage is divided into 13 layers in order to simulate the real condition accurately as much as possible (red rectangles). Gray area highlights the spatial region where the real value of permittivity acquires values between -1 and 1 representing the ENZ region.

3.1.2 Gap plasmon polaritons and bulk plasmon polaritons

Based on this unique characteristics, optical mode engineering is carried out. According to electronic characteristics of the MOS capacitor of the proposed device introduced in the previous section, there are limitations of modulation using ITO such as too small refractive index change and too thin thickness of accumulation layer. To enhance light-active material interaction and expand functionalities, the proposed device relies mainly on gap plasmon polaritons (GPPs) and bulk plasmon polaritons (BPPs),

different kinds of strongly confined high- k modes [65]. Figure 3.3 represents mode profiles of three optical modes shown in the proposed structure. First of all, a MIM waveguide consisting of Au gratings and the top Au layer of HMM supports GPP mode which has extremely high modal index (left panel of Figure 3.3). Note that black arrows indicating surface currents form a current loop that induces magnetic field and flow along the parallel direction. In this case, incident wave feels HMM as metal ($\epsilon_{\parallel} < 0$), thus cannot penetrate inside HMM. Due to a merit to induce strong light-matter interaction, this kind of configuration has attracted considerable attention for use in nanophotonic applications such as a perfect absorber [27,28,42,43,55]. The thickness of HfO₂ and ITO are respectively chosen to be 10 nm and 20 nm which are sufficiently thin since the modal index is approximately inversely proportional to the gap size between metal layers [66]. Most of the previously reported studies on TCO-based modulators have used GPP mode to control the amplitude or phase of reflected light due to its high modal index [27,28,42,43].

On the other hand, BPP mode, a different kind of highly confined mode that can be only observed with HMM substrate, is excited within HMM substrate unlike GPP mode (center panel of Figure 3.3). This mode is induced from SPPs excited at the interface between Au grating and HfO₂. In general, SPP mode has a long tail to dielectric material and very short penetration depth to metal (right panel of Figure 3.3). However, the evanescent field of SPPs can be easily coupled to HMM owing to the thin

thickness of metal and dielectric layers in HMM. Moreover, SPP wave oscillates along the parallel direction, thus this mode feels HMM as high refractive index dielectric material ($\epsilon_{\perp} > 0$).

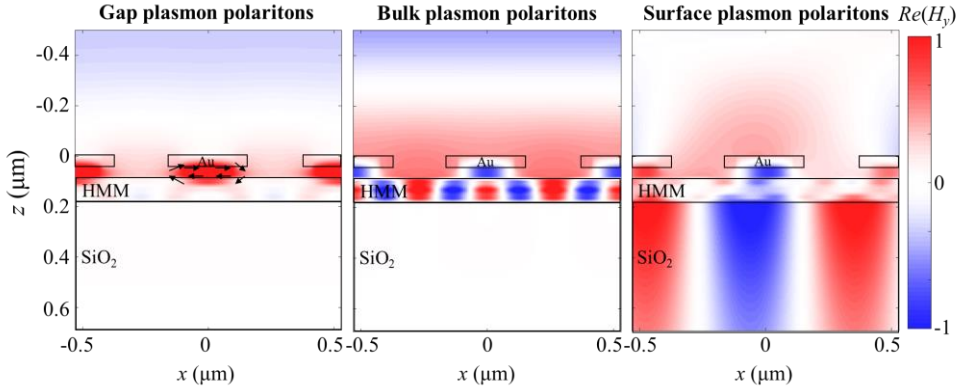


Figure 3.3. Three kinds of high- k modes. The spatial distribution of y -component of magnetic field at gap plasmon (left panel), bulk plasmon (center panel), and surface plasmon (right panel) resonance.

These high- k modes including GPP and BPP supported by the proposed device can be intuitively explained by calculating the dispersion relation. The reflectance is calculated at different wavelengths and wavevectors for two cases: the proposed design (left panel of Figure 3.4) and simple MOS capacitor without HMM substrate (right panel of Figure 3.4). The period, width and thickness of the nanogratings are respectively chosen as $p = 530$ nm, $w = 230$ nm, and $t_g = 50$ nm to design the spectral position of the gap plasmon (GP) resonance at NIR frequencies. In both cases, surface plasmon (SP) resonance is observed between 1000 nm and 1100 nm. This mode is excited at the Au-SiO₂ interface. The reflectance of SP resonance in the

proposed structure is lower than that of the case without HMM due to the energy loss from coupling with the metal-dielectric multilayer. More importantly, there is a GP resonance around 1500 nm of wavelength, and the proposed device acts as a perfect absorber at these wavelengths. These results imply two important properties; GPP mode is not affected by additional changes in structure such as the set number of multilayer, and not sensitive to wavevector of the incidence. It is because this GPP is like localized resonance, not related to the structure of the lateral period but only to the geometric parameters of the grating and thickness of the dielectric layer. On the other hand, it is confirmed that BPP modes are supported by metal-dielectric multilayer (left panel of Figure 3.4), and sensitive to the wavevector of the incidence. It means that the resonance characteristics of BPP modes can be tuned by changing the angle of incidence while those of GPP modes remain unchanged. Therefore, based on two different kinds of high- k modes, different kinds of functions can be implemented on a single platform depending on the angle of incidence.

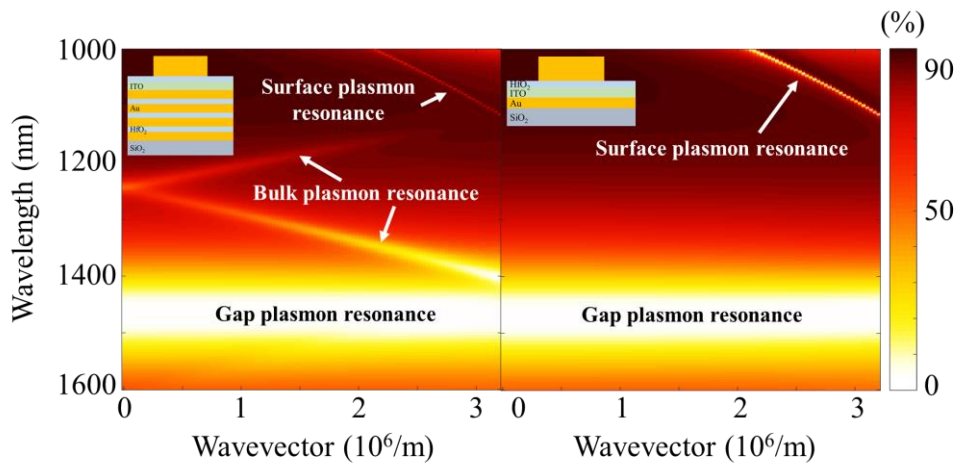


Figure 3.4. Dispersion relation of the proposed structure. Color map of the simulated reflectance versus wavevector and wavelength for the proposed structure (left panel) and the structure without HMM in the proposed one (right panel). The various types of resonance are named (Insets: structure diagrams).

3.2 Phase modulation with normal incidence

Let us think about the situation where a wave is normally incident with transverse magnetic (TM) polarization along the z -direction. In this case, nearly perfect absorption phenomenon by GPP modes in the NIR range is utilized to modulate the phase of reflected light. Figure 3.5a shows the reflectance spectra as a function of wavelength for different applied voltages. The resonance dip shifts to shorter wavelengths as the applied bias increases due to reduction of the value of real permittivity. From the wavelength of 1450 to 1460 nm, the device absorbs almost all the incident light regardless of the changing applied voltage. As shown in Figure 3.3, the electric field does not penetrate into HMM and light is highly confined between the metal grating and the topmost metal layer. The GPP mode is formed on ITO and HfO_2 layers between Au nanogratings and HMM. It means that the incidence feels the HMM substrate as a metal layer. As discussed in the previous section, the resonance is not affected by external changes such as the wavevector of incidence or the number of multilayer since the momentum matching conditions to excite GPP mode in the MOS capacitor are already satisfied at the resonant wavelength, which leads to nearly constant reflectance value.

To observe the phase shift of reflected light more intuitively, complex reflectance as a function of applied voltage from -2 to 3 V for target

wavelength of 1450 nm is plotted in Figure 3.5b. In the complex map, the distance from the origin is related to the absolute value of reflectance, and the angle with respect to real axis means the phase of the reflected wave. In other words, phase modulation depth can be calculated using the shifted angle and the applied voltage around the origin. The complex reflectance shows a tendency to move along the trace of the curve in the clockwise direction regardless of the wavelength of incidence as the voltage increases. Basically, the variation of complex reflectance due to the voltage application is not large since the permittivity of the material changes only in a very thin region. In order to enable large phase modulation with such small changes, the variation of complex reflectance must occur near the origin, and the curve has to turn around the origin. Therefore, a wide range of phase modulation can only occur near the perfect absorption condition. Moreover, it has a wide bandwidth of approximately 20 nm under the condition of π -phase modulation due to broad bandwidth characteristics of GPP mode. The simulation results show that the proposed device can modulate the phase of reflected light with about 207 degrees of modulation depth at the operation wavelength of 1450 nm for normal incidence, whereas the amplitude is almost fixed around 1.7 % (Figure 3.5c). For more intuitively comprehension, the phase shift is visualized in Figure 3.5d. These field distributions represent the case of applied voltages of -2 V (left panel) and 3 V (right panel), respectively.

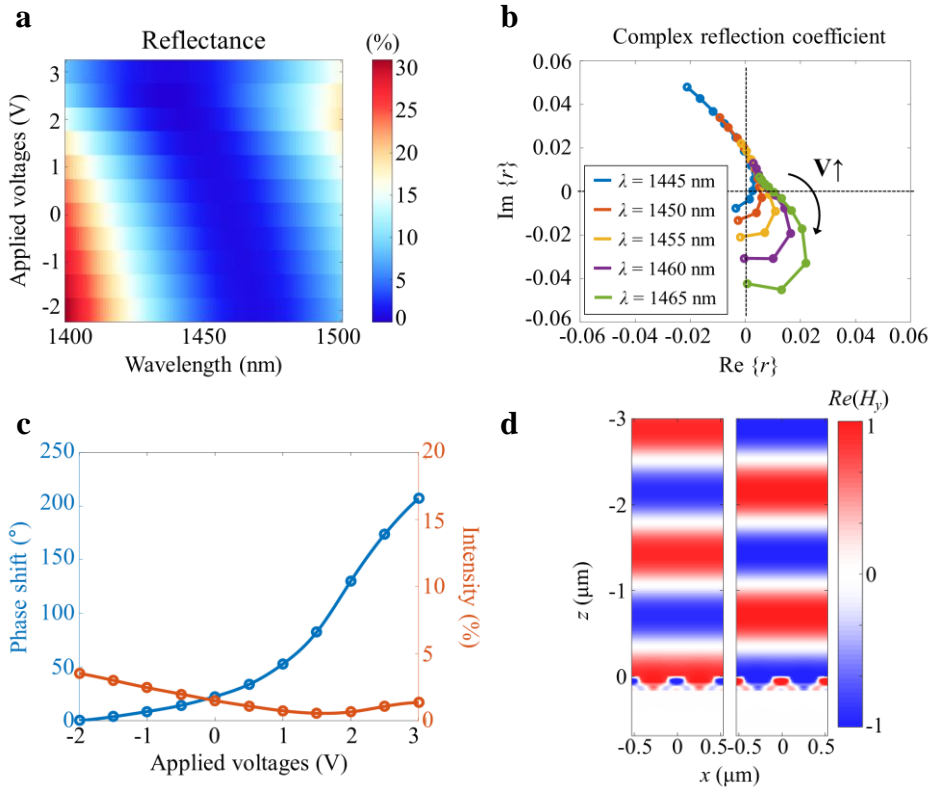


Figure 3.5. For normal incidence, (a) Color map of the reflectance versus wavelength and applied voltages. (b) Calculated complex reflectance as a function of applied voltages for the wavelength of 1450 nm. Applied voltage increases along the clockwise direction. (c) Simulated phase shift and intensity as a function of applied voltages at target wavelength of 1450 nm. (d) The spatial distribution of y -component of magnetic field of reflected light when the applied voltage is -2 V (left panel) and 3 V (right panel).

3.3 Amplitude modulation with oblique incidence

Now, let us consider the case of oblique incidence on the same structural condition. With TM polarization, the incident light can have a momentum of $n_0k_0\sin\theta$ as the incidence angle is θ , and such momentum compensation by oblique incidence can excite several new types of modes that are not seen in normal incidence. To implement different types of modulation at the same operating wavelength, it is important to design the BPP modes to be as close to the wavelength as possible with the GPP mode. It can be engineered by adjusting the number of added metal-dielectric layers and the incident angle without affecting the GPP modes.

First, Figure 3.6a represents the reflectance spectra as a function of wavelength for changing the number of sets in HMM. These BPP modes occur at shorter wavelengths as the number of sets in HMM increases. This is because as the number of layers increases, the number of nodes in the field increases which requires a higher energy level to induce the BPP modes. Then, the reflectance spectra as a function of wavelength for different incident angles are calculated (Figure 3.6b). In this calculation, it is assumed that the HMM consists of 3 sets of Au-HfO₂ multilayers. Note that as the angle of incidence increases, the wavelength at which same order BPP resonance occurs becomes longer. It is reasonable that the wavenumber in vacuum k_0 gets smaller as the sine value of angle increases because the

amount of momentum needed to form this kind of mode is constant. This interpretation applies equally to SPP excited at the Au-SiO₂ interface with a sharp resonance dip. As a result, the proposed modulator has another kind of resonance mode near the operating wavelength by introducing oblique incidence of 60 degrees. Unlike GPP modes, these kinds of modes are formed when the constructive interference between the waves guided from both lateral structures occurs, thus the x -component of the wavevector is key factor to determine the resonance characteristics. It is evident that the electric field penetrates into the metal-dielectric multilayer and is confined on the dielectric layers in HMM (Figure 3.6b). The mode profile shown in the y -component of the magnetic field indicates that the mode is formed in the whole structure including HMM, and it is supported by a nanoscale multilayer as well as the MOS capacitor.

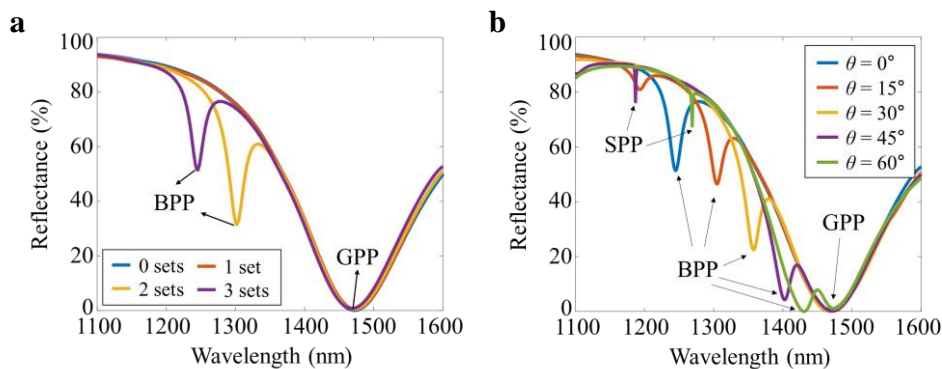


Figure 3.6. The reflectance spectra (a) for the multiple Au-HfO₂ sets in HMM with normal incidence and (b) as a function of the incident angles with the proposed structure. Several resonances are classified by types.

Figure 3.7a represents the reflectance spectra for different wavelengths and applied voltages. There are two resonance dips, BPP mode at around 1420 nm of wavelength and GPP mode at around 1470 nm of wavelength as discussed above. Note that the intensity varies in case of GPP mode depending on the applied voltages while BPP mode absorbs almost the entire incidence regardless of the applied voltages. This is because by bringing the GPP mode closer to the BPP mode, perfect absorption by GP resonance breaks, and GP resonance becomes unstable by interference between two high- k modes. Complex reflectance as a function of applied voltage from -2 to 3 V for target wavelength of 1450 nm is depicted in Figure 3.7b. Similar to the phase modulation case, each curve moves in the clockwise direction depending on the applied bias. Around the BP resonance wavelength, the complex reflection coefficient moves near the origin. On the other hand, in case of GP resonance at around 1450 nm, the values of complex reflection coefficients are away from the origin; thus, the curve no longer forms a shape to move around the origin. Therefore, as the applied voltage varies, the distance from the origin is changed greatly compared to the phase modulation case, while the phase shift is restricted. At the operation wavelength of 1450 nm, the proposed device can modulate the reflectance with ~ 6.8 % of modulation depth (defined as $\Delta R(\lambda) = R(\lambda)_{V=3} - R(\lambda)_{V=-2}$), and ~ 86 % of relative reflectance change (defined as $\Delta R/R_{V=-2}$) while the phase shift is restricted below 16 degrees in Figure 3.7c. The

intensities of magnetic fields for applied voltages of -2 V (left panel) and 3 V (right panel) confirm that the amplitude of the reflected light is modulated in Figure 3.7d.

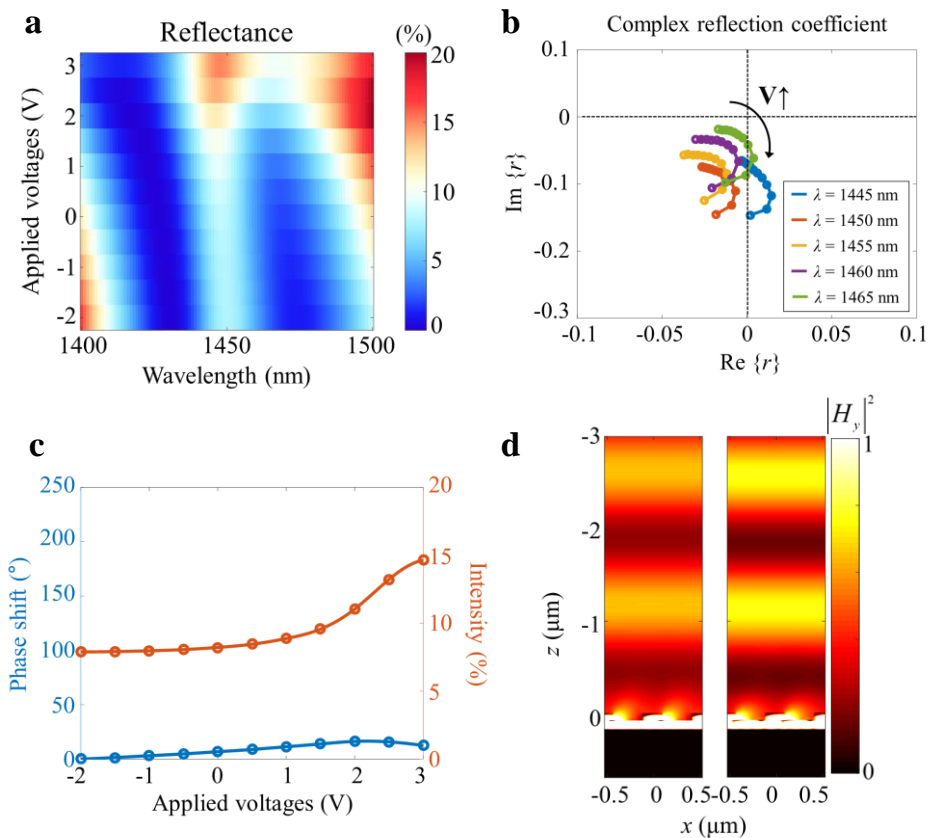


Figure 3.7. For oblique incidence of 60° , (a) color map of the reflectance versus wavelength and applied voltages. (b) Calculated complex reflectance as a function of applied voltages for target wavelength of 1450 nm. Applied voltage increases along the clockwise direction. (c) Simulated phase shift and intensity as a function of applied voltages at operating wavelength of 1450 nm. (d) The intensity of magnetic field of reflected light when the applied voltage is -2 V (left panel) and 3 V (right panel).

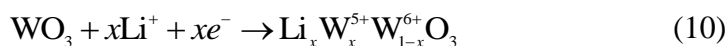
3.4 Conclusion

In conclusion, a numerical demonstration of an electrically tunable multifunctional device in the NIR region is reported. The nanoscale MOS capacitor including ITO layer is introduced for implementation of electrical-driven device. Furthermore, by combining an HMM configuration, the proposed modulator was designed to have different kinds of high- k modes, BPP modes in HMM region, depending on the angle of incidence. The proposed device acts like a phase modulator with normal incidence using GPP mode formed in MOS capacitor, whereas it shows amplitude modulation with oblique incidence using the resonance coupling of GPP and BPP modes formed inside HMM substrate. It is expected that the proposed mechanism in optical mode engineering can open a new pathway to design practical multifunctional applications such as miniaturized multi-sensing systems and spatial light modulators capable of phase and amplitude modulation for the next generation ultracompact integrated optical systems.

Chapter 4. Full-color-tunable electrochromic device using WO₃ thin film

4.1 Tungsten trioxide as an electrochromic material

WO₃ is a well-known ion conducting oxide of which electrochemical performance is applicable for batteries and supercapacitors. WO₃ itself is electronically insulating material. However, its ionic conductivity is originated from their ReO₃-type structure (empty perovskite). It has pores and voids between corner-sharing WO₃-octahedras, so the ion transport and intercalation are possible by the following reaction.



For monoclinic WO₃, change in crystallinity was reported during the cationic charging. At lower charging state ($x < 0.1$), cations intercalate without changing monoclinic WO₃ frame. The monoclinic WO₃ is changed to orthorhombic, tetragonal, and cubic structure as the amount of intercalated cations are increased. Not only the crystal structure, but also the electronic conductivity is changed along with the charging state: insulator to semiconductor ($x \approx 0.25$), and semiconductor to metal ($x \approx 0.4$).

WO₃ is used without further purification. WO₃ thin film is deposited by

radio frequency sputter without further thermal annealing. The WO_3 powder was placed on Cu back plate and pressed with ~ 6.5 Mpa pressure. The base pressure in the sputter chamber was set to below 1×10^{-5} Torr. The partial pressure during sputtering was set to 7 mTorr for Ar, and RF power is fixed to 100 W. In this condition, O_2 is supplied additionally with 2 sccm flow rate, then working pressure of chamber becomes 8.3×10^{-3} torr. The distance between substrate and target is determined as 10 cm for reflection type and 14 cm for transmission type. This is because the substrate of transmission type, Ag, is vulnerable to the collision of Ar ions. The sputtering conditions summarized in Table 4.1.

Target	WO_3 (99.9 %)
Base pressure	1×10^{-5} torr
RF power	100 W
Working pressure	8.2×10^{-3} torr
Substrate temperature	Room temperature
Gas	Ar + O_2 (2 sccm)
Distance between substrate and target	10 cm (reflection type) / 14 cm (transmission type)

Table 4.1. Sputtering conditions for WO_3 thin film deposition

The electrochemical experiment was conducted by employing three-electrode cell with an Ag quasi reference electrode (Ag wire in 10 mM AgNO_3 dissolved in acetonitrile) and a Pt plate as a counter electrode. 100 mM of LiClO_4 in acetonitrile solvent was used for electrolyte. For electrical contact of WO_3/Si electrode, the backside of Si was scratched by diamond point pen, and gallium-indium eutectic ($\geq 99.99\%$ trace metals basis from

Sigma-Aldrich) was applied to the scratched region. Finally a 10-cm-long conductive adhesive tape was attached on the gallium-indium eutectic. The potentiostatic and galvanostatic analysis of WO_3/Si electrode were conducted by a commercial instrument of Reference 600 (Gamry Instrument, US). For galvanostatic intermittent titration (GITT) experiment, -1.78 mA/cm^2 was applied to intercalate Li^+ for 5 s, and then system was rested in open circuit condition for 55 s to achieve steady state potential. Cyclic voltammogram was obtained with varying scan rate from 5 to 500 mV/s. For ex-situ and in-situ optical measurement under potential bias, mobile potentiostat, Compactstat (Ivium Technologies, The Netherlands), was employed.

Before the electrochemical analysis, cyclic voltammograms (CV) was carried out from 1 V to -1.5 V for making electrical connection between the WO_3 and underlying the Si electrode because there is SiO_x layer generated in between WO_3 and Si during sputtering which blocks current. After several CV cycles, voltammograms converge on a specific curve and the color change became uniform over the exposed area, confirming sufficient conduction pathway was made between WO_3 and Si induced by dielectric breakdown of SiO_x . The WO_3 film shows Li capacity at the potential more negative than 0.5 V vs. Ag/Ag^+ reference electrode as shown in the CV conducted at 5 mV/s (Figure 4.1). The current density and the film thickness shows positive relationship, because the Li capacity is proportional to the thickness of the WO_3 . In case of the 364-nm-thick WO_3 , Li

charging/discharging characteristics deviate more from ideal capacitor behaviors due to the increasing resistance of the film. Also, CV obtained at higher scan rates (50 to 500 mV/s) are presented in Figure 4.1, which shows ohmic character with a scan rate dependence of current, $b = 0.099$ in $i = a(dV/dt)^b$.

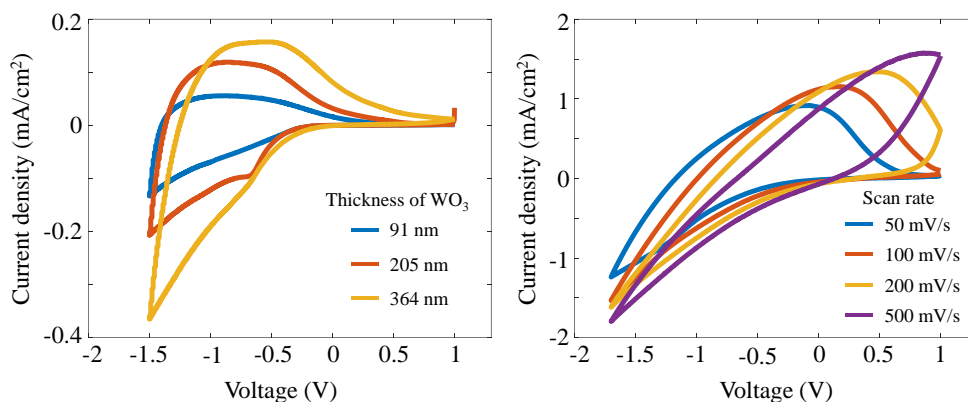


Figure 4.1. Cyclic voltammograms in 100 mM LiClO₄ electrolyte (acetonitrile) for different (a) the film thicknesses and (b) scan rates.

This quasi-capacitive character would be resulted from the diffusivity of Li in WO₃. Phase change of Li conducting oxides was via CV in previous literatures, however, no obvious feature was observed, showing that the amorphous nature of WO₃. Nevertheless, the phase change of the film can be deduced by the reduced overpotential for Li intercalation at higher scan rates, which means the residual Li that could not escape from the film facilitates the Li intercalation kinetics.

The steady state potential versus stoichiometry, x , of Li _{x} WO₃ and diffusivity

of Li versus x were obtained by galvanostatic intermittent titration technique (GITT) conducted at various compositions (Figure 4.2). GITT is a useful technique to find out the diffusivity of foreign species that can intercalate into the thin layer. In GITT experiment, current ramp is applied for short time period to intercalate the species, Li⁺ in this work. By relaxing the system at open circuit condition for enough long time, the steady state potential for certain stoichiometry can be obtained. The steady state potential shows linear relationship to x , utilizing the voltage ramp to modulate the amount of Li in device operation. The diffusion coefficient (D) is extracted from the slope of coulometric titration curve at open circuit relaxing condition (steady state potential versus Li content) and chronopotentiometric curve at current ramp period (cell potential versus square route of time) [67]. Then the equation for D is derived to be

$$D = \frac{4}{\pi} \left(\frac{m_B V_M}{M_B S} \right)^2 \left[\frac{\Delta E_s}{\tau (dE / d\sqrt{t})} \right]^2 \quad (11)$$

where m_B , M_B , and V_M is the mass, the atomic mass and molar volume of WO₃, S is the area of the WO₃ film, E_s is the slope of coulometric titration curve, τ is the time of current ramp, and E is the cell potential during the current ramp period.

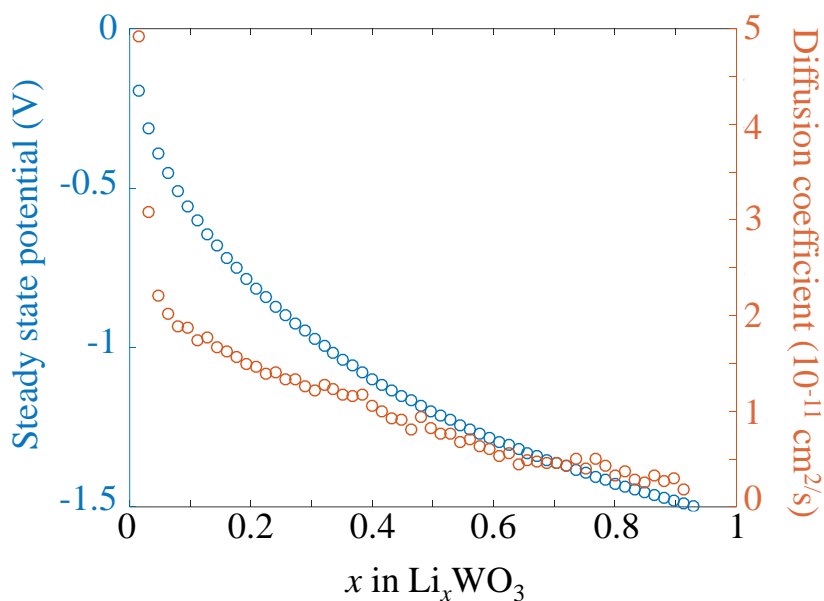


Figure 4.2. Steady state potential and diffusion coefficient as a function of x in Li_xWO_3 via galvanostatic intermittent titration technique (GITT).

D was $4.91 \times 10^{-11} \text{ cm}^2 \text{ s}^{-1}$ at $x = 0.03$ and D decreased with x (Figure 4.2). Slow diffusion in higher Li content can be found in other literatures, which could be ascribed to the repulsion of Li in WO_3 matrix. According to the literature, the intercalation capacity is 0.5 Li per formula unit for bulk (crystal structure) WO_3 and 1.12 for WO_3 nanorod. However, Li capacity of our WO_3 film was ~ 0.9 and the voltametric response was reversible despite the high electrochemical stress induced to the film.

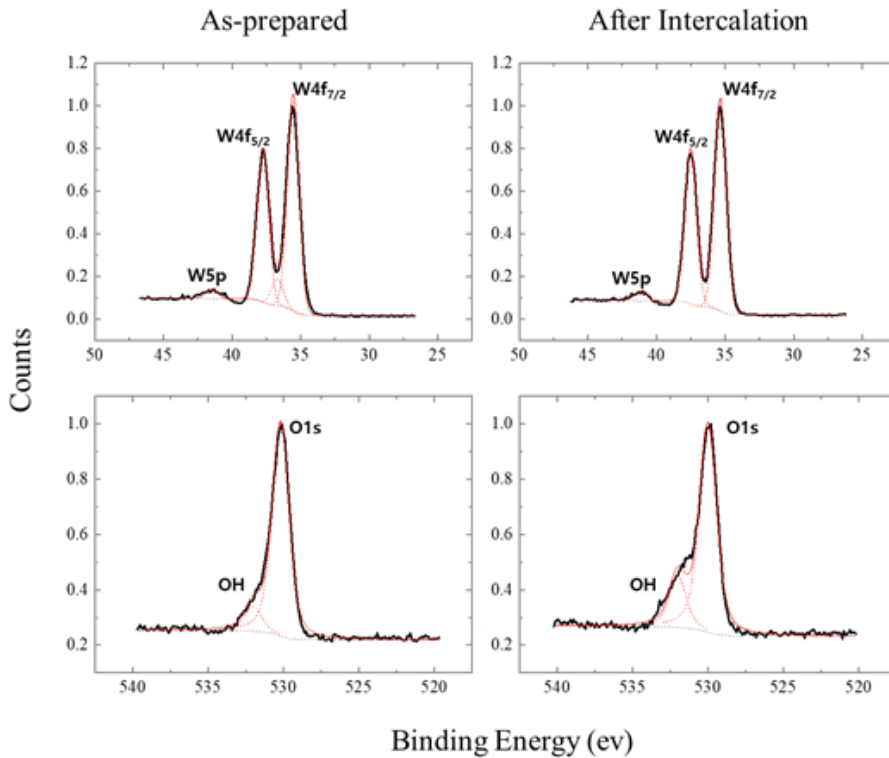


Figure 4.3. X-ray photoelectron spectra of (left) as-prepared WO_3 film in the region of W (upper-left) and O (bottom-left). X-ray photoelectron spectra of WO_3 after Li intercalation are presented on the right column in the region of W (upper-right) and O (bottom-right).

The amorphous film was expected to be obtained due to no further annealing after deposition. The structure of WO_3 film is characterized by X-ray photoelectron spectroscopy (XPS) (Figure 4.3) and X-ray diffraction (XRD) (Figure 4.4). XPS spectra clearly confirms the identity of film to be tungsten trioxide, which has a little oxygen deficiency ($\text{WO}_{2.7}$) [68]. The deficiency would be originated from the insufficient amount of oxygen gas in the sputter chamber, however, oxygen partial pressure is set to be below

1.5 mTorr for preventing a possible oxidation damage of substrates. A shoulder arises on the O_{2p} band obtained at the surface of WO_3 after the Li intercalation in acetonitrile, which infers that the surface oxygen is reduced to hydroxyl group. The surface hydroxyl group would be resulted from the inevitable water content in organic solvents, however the wetting was not observed at the bulk region. XRD pattern of WO_3 film shows broad peaks of (200), (022), (202), which show its amorphous nature.

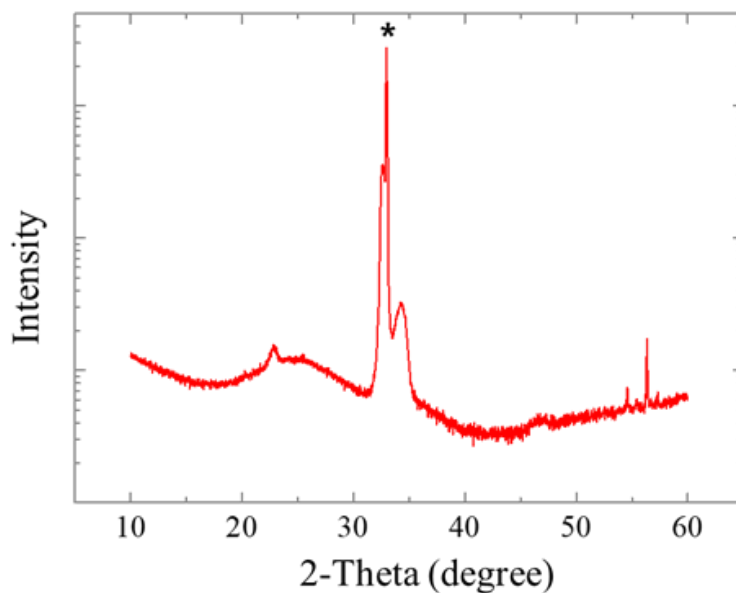


Figure 4.4. X-ray diffraction spectrum of WO_3 thin film deposited on highly doped Si wafer.

Morphology analysis was conducted with scanning electron microscopy (SEM). As shown in Figure 4.5, as prepared amorphous WO_3 film has flat and smooth surface. Cracks are generated after repetitive

charging and discharging, however, the roughness of single domain divided by cracks does not change. This topological change would be resulted from the mechanical strain applied to WO_3 film. During the charging/discharging processes, the volumetric change of monoclinic WO_3 crystal structure is known to be 17%. Considering the amorphous WO_3 film comprised of the locally crystalline WO_3 clusters, the topological strain due to the ion intercalation would be less than that of crystalline WO_3 . The generated cracks are the result of deformation, which is a stabilized structure that compensates for mechanical stress.

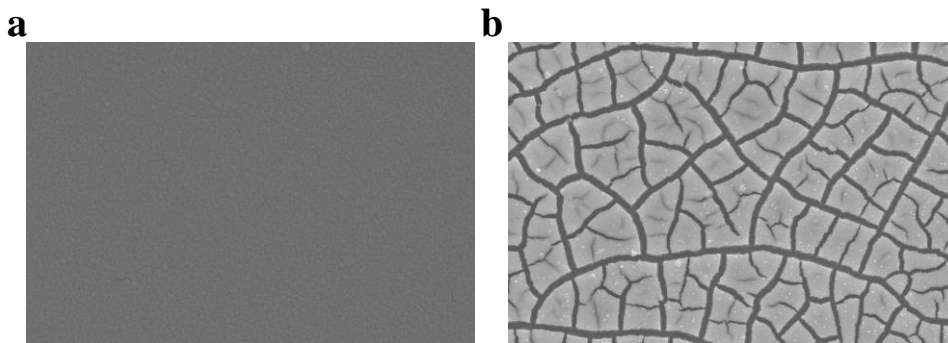


Figure 4.5. Scanning electron microscopy image of (a) as-sputtered WO_3 film and (b) WO_3 after Li intercalation/de-intercalation cycle.

To obtain optical properties of WO_3 thin films incorporated in the proposed device, WO_3 -on-Si samples are fabricated for ellipsometry measurement. The sputtered WO_3 films are characterized, not only in the extreme bleached and colored states, but also a range of intermediate charge

states. The refractive index (n) and absorption coefficient (k) are measured at coloration states corresponding to injected volumetric charge densities of 0, 6, 22, 38, 46, and 80 mC cm⁻² μm⁻¹ which correspond to the Li content, x , of 0, 0.025, 0.088, 0.14, 0.18, and 0.32, respectively (Figure 4.6). V-VASE spectroscopic ellipsometer system (J. A. Woollam, US) was used. Each state is called state 1 to 6 for convenience. One can see that the n and k change sufficiently to be exploited as color display by Li⁺ intercalation. In the visible regime, as the higher charge-injected state, the measured results show a tendency of decreasing n and increasing k . In particular, the change of k by ion injection becomes much larger as the wavelength gets longer. This property is directly related to the fact that the extreme color state after sufficient charge injection with WO₃ is typically deep blue. Although there is topological change after Li intercalation/de-intercalation cycles, the voltammetric response and optical properties are reversible during the repetitive Li transportation. This reversibility, which would be ascribed to the structural stabilization by micrometer-scale domains created after the Li intercalation/de-intercalation cycles, is a critical advantage for practical device operation. Therefore, we could conclude that the a-WO₃ film is suitable for electrochemically tunable optical device which employs sophisticated structure for better optical performance.

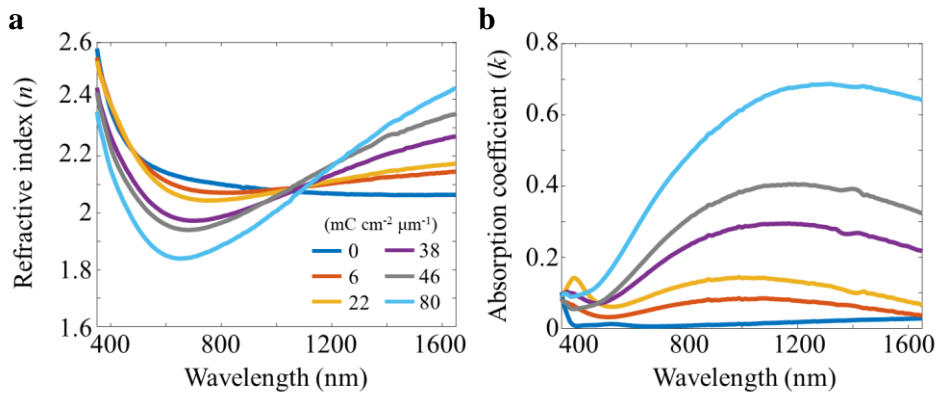


Figure 4.6. The optical properties of WO₃ thin film as a function of the amount of Li⁺ injection. (a) Refractive index and (b) absorption coefficient are measured with a range of wavelength from 350 nm to 1650 nm.

4.2 Reflection-type electrochromic device and color tuning

The reflective type of display using WO_3 thin films is described in this section. The cross-sectional schematic of the reflective devices, only the WO_3 thin film deposited on a highly doped Si substrate serving as a reflector and an electrode, is depicted in Figure 4.7. The reflected light in the bleached-state WO_3 on Si represents specific color, and its color can be tuned as WO_3 changes to Li_xWO_3 by Li^+ intercalation. The refractive index of WO_3 immersed in LiClO_4 ($n = 1.34$) varies by applied voltages between the Si substrate and the electrolyte, which results in the visible spectrum change. The optical resonance occurs when the reflected light on the boundaries of electrolyte / WO_3 and WO_3 / reflector interferes constructively and forms a cavity mode inside WO_3 film. This resonance leads to a reflectance decrease due to energy confinement in cavity. The thickness of WO_3 (t) as a cavity determines the resonant wavelength so that a desired color generation can be achieved with this spectrum engineering by t . In this configuration, the key point of design is to maximize reflectance in the wavelength region of the desired color, while to suppress reflectance by placing the resonance in the unwanted region. In this respect, most noble metals that have extremely low refractive indices and high absorption coefficient are inappropriate to be utilized as a reflector for the proposed device because they show high reflectivity compared to the reflectivity on

the electrolyte / WO_3 interface. The reflectivity can be simply calculated by Fresnel equation with normal incidence as $R = \left(\frac{n_1 - n_2}{n_1 + n_2} \right)^2$, where n_1 and n_2 correspond to the refractive index of the different media, respectively. In case that noble metals are utilized as a reflector, it is difficult to expect nearly zero reflectance under the resonance conditions. This means that the light of unwanted wavelength region cannot be completely eliminated and the color of reflected light is blurred. For this reason, a highly doped Si is selected as an excellent candidate as a reflector in the proposed device due to its moderate reflectivity and conductivity to be used as an electrode.

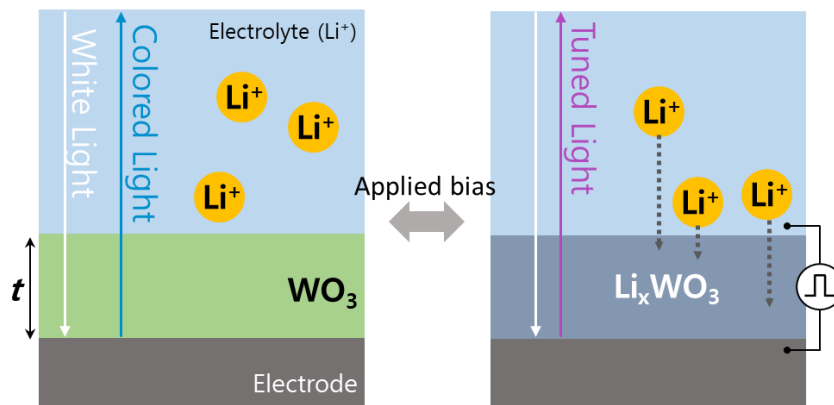


Figure 4.7. The schematic illustration of reflection-type color generation and tuning.

Based on the optical properties of WO_3 , the spectra of reflected light are calculated for different film thicknesses (Figure 4.8a). Several orders of cavity resonance are seen. Spectrum for desired color can be engineered by choosing proper film thickness. Therefore, the thicknesses of WO_3 thin film

(t) are respectively determined as 165 nm, 230 nm, and 205 nm for red, green, and blue (Figure 4.8b).

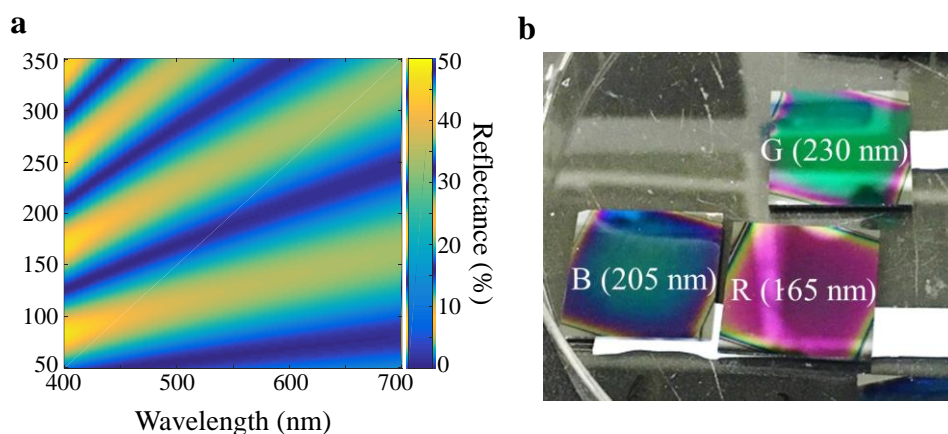


Figure 4.8. (a) Reflectance of WO₃ thin film on Si as a function of the incident wavelength and the thickness of WO₃. (b) Photographic image of fabricated red, green, and blue samples with target thickness.

Three primary colors generation (red, green, and blue) and their color tuning by Li⁺ injection are numerically calculated (top of Figure 4.9). Color variations corresponding to each same colored spectrum proceed from state 1 through 4 to 6 (inset of Figure 4.9). For all colors, the resonant dips show blue-shift for Li⁺ injection due to decrease of refractive indices of WO₃. After WO₃ deposition to the target thicknesses on the highly doped Si substrate, the spectra of reflected light are measured using a solar simulator (10500, Abet Technologies) as a broadband source (bottom of Figure 4.9). The incident light is focused onto the WO₃ surface by using a 10×, 0.25 NA microscope objective. The light reflected from the WO₃ sample is diverted

by a beam splitter and sent to visible camera or an optical spectrometer (Acton SP2300). The measured reflectance is normalized relative to light reflected directly from the mirror. Figure 4.9 shows exceptionally good agreement between the simulated and experimental reflectance spectra for all three colors.

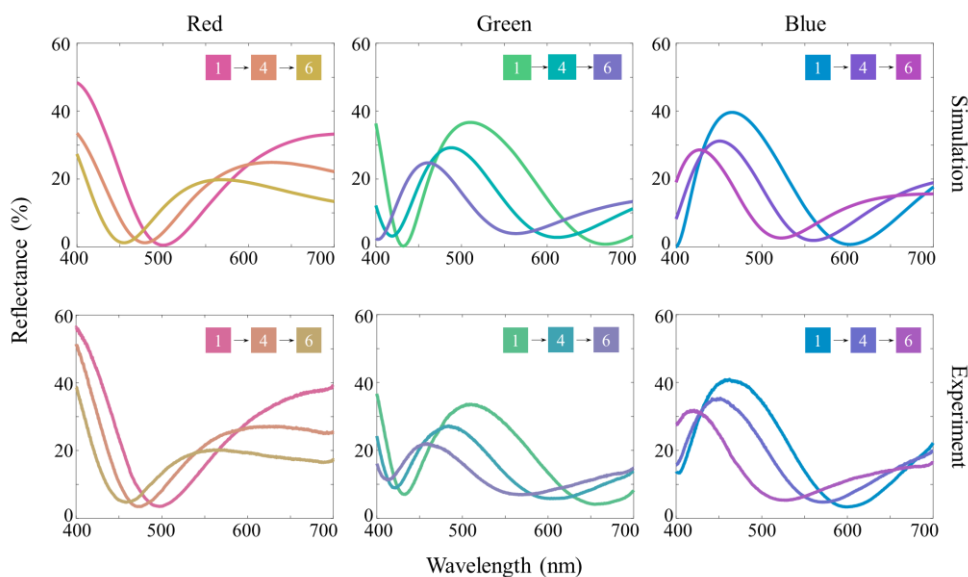


Figure 4.9. Calculated (top) and experimental (bottom) spectra of reflected light. Color variation corresponding to each same colored spectrum from state 1 through 4 to 6 (inset).

Also, it is verified with additional experiments that the fabricated WO_3 is sufficiently reversible and stable to be utilized as color display elements. Above all, to verify the electromagnetic reversibility of fabricated thin film, Li^+ -charging and -discharging into 235 nm thick- WO_3 (green) are repeatedly carried out from state 1 to state 6 in three-electrode-electrochemical system.

The optical spectra of the reflected light are observed for state 1 and 6 after repeating 40 times, and 80 times under the voltage application range of 0.5 V to -1.5 V. In both cases, the measured spectrum shows red-shift as increasing the number of repetitions (Figure 4.10a and 4.10b). During the repeat of Li^+ intercalation, the local volume randomly changes, and the amorphous phase can also be partially poly-crystalline. This is why it appears that the oxidation of WO_3 takes place in the existing state.

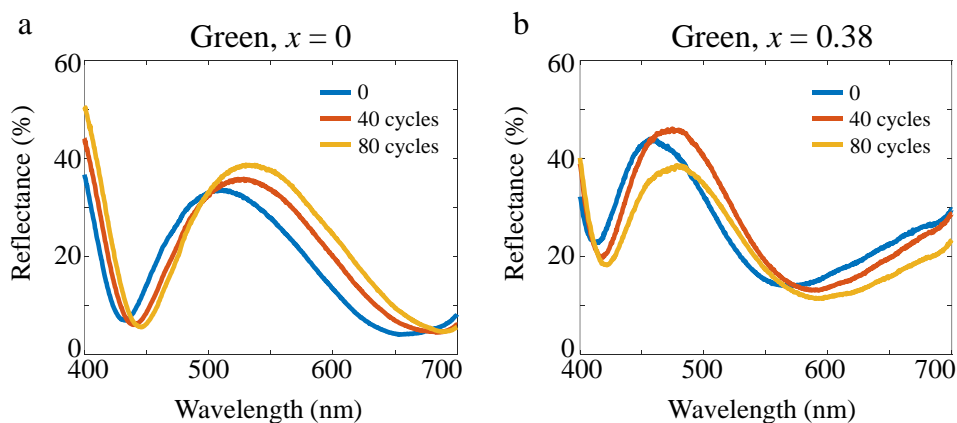


Figure 4.10. The reversibility and stability test of the WO_3 -based structure. The spectrum change of a 235-nm-thick WO_3 on Si of state (a) $x = 0$ and (b) $x = 0.38$ for different Li^+ intercalation cycles.

Meanwhile, WO_3 immersed in electrolyte is more susceptible to oxidation or reduction than in the air since this device works in electrolyte with enormous amount of charge. The proposed device based on electrochemical control is not perfectly non-volatile type, however coloration state is maintained for a long enough time without external

supplying energy. To test the stability our device, first of all, the $80 \text{ mCcm}^{-2} \mu\text{m}^{-1}$ Li^+ ions are injected into the 165 nm thick- WO_3 on Si (red) to make the coloration state 6. The sample has been immersed in LiClO_4 for a few time conditions (1 h, 1.5 h, 18 h, and 24 h) without any applied voltage, and the spectral changes of reflected light are measured at each time (Figure 4.11). Over time, the coloration state 6 tends to return to original state 1, and shows red-shift. After 24 hours, the measured spectrum indicates that the sample has almost returned to the state 2. WO_3 film is like battery, thus it can be interpreted that self-discharge occurs in electrolyte.

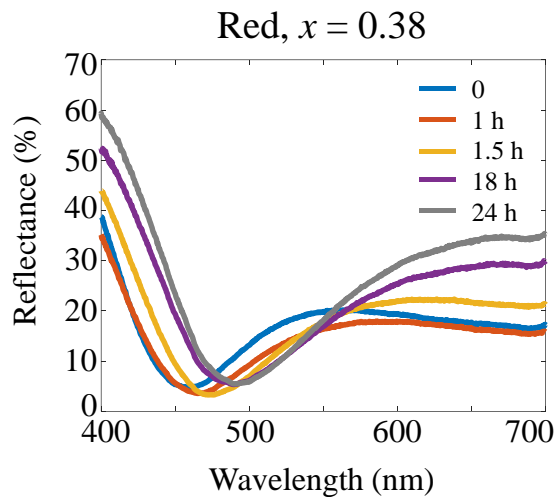


Figure 4.11. The reflected spectra of a 165-nm-thick WO_3 on Si of state 6 for different time conditions immersed in electrolyte.

4.3 Color-purified transmission-type electrochromic device

Reflection type display discussed in previous section has distinct advantages of simple structure and a large contact area with the electrolyte, which leads to a short reaction time, but has a problem of poor color purity. In this section, the transmission type color display based on WO₃ thin film is suggested. For centimeter-scale display applications, complex nano-fabrication is excluded and the purity of color is enhanced with simple film depositions.

Figure 4.12 shows the cross-sectional schematic and SEM images of the transmissive type devices; the WO₃ is sandwiched between two 40 nm-thick Ag layers on quartz substrate. The transmittance of this metal-insulator-metal configuration with normal incidence is well known as follow:

$$T = \frac{1}{1 + \frac{4R \sin^2 nk_0 d}{(1-R)^2}}. \quad (12)$$

In Equation 12, R is power reflectance at the Ag / WO₃ interface, n is the real part of refractive index of WO₃, and d is the thickness of WO₃, respectively. When light is incident on the structure, reflected light on each Ag layer causes interference, and the Fabry-Pérot (FP) resonance occurs on the condition of constructive interference as $m\lambda = 2nd$ in Equation 12, where

m is the order of interference, λ is the wavelength of incidence. Under the normal incidence, the thickness of WO_3 (d) sandwiched by Ag layers determines the resonant wavelength. In particular, the finesse (F) directly related to R is defined as,

$$F = \frac{\pi\sqrt{R}}{1-R} \quad (13)$$

It can be seen that by increasing the reflectance at the WO_3 / Ag interface, the full width at half maximum (FWHM) of the proposed color filter can be much narrower and the purity of color can be enhanced.

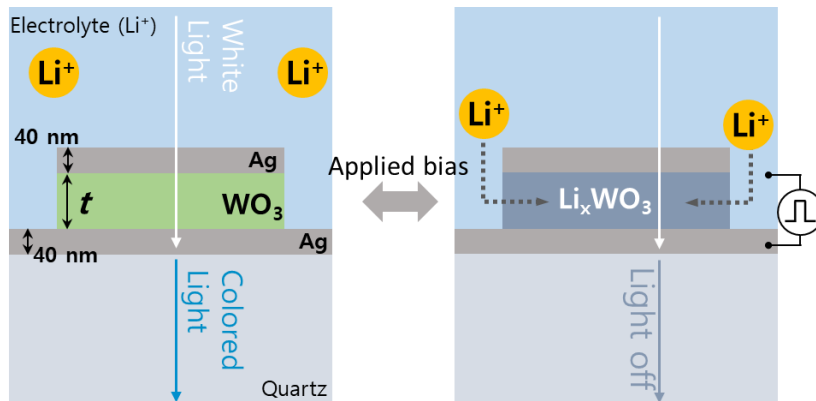


Figure 4.12. The schematic illustration of transmissive type electrochromic device. The working principle is described.

The transmittance as a function of the thickness of WO_3 and the wavelength of incidence is numerically calculated with the thickness of Ag fixed at 40 nm (Figure 4.13a). The overall shape of the resonance is almost the same as the reflection type. However, due to high F from reflectivity of Ag, the FWHM of resonance is highly narrower, resulting in enhanced color

purity. For three primary color generation, the thickness of WO_3 is determined as 100 nm, 70 nm, and 50 nm, respectively (Figure 4.13b).

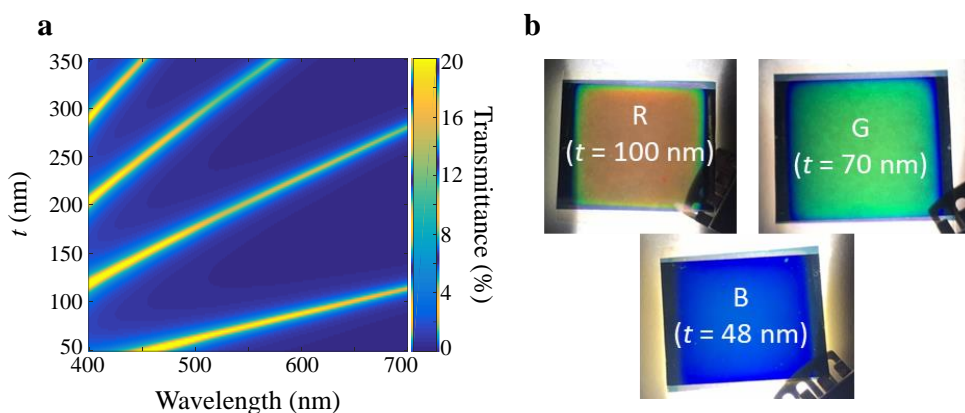


Figure 4.13. (a) Transmittance of $\text{Ag}/\text{WO}_3/\text{Ag}$ on quartz substrate as a function of the incident wavelength and the thickness of WO_3 . (b) Photographic image of fabricated red, green, and blue samples with target thickness.

For transmission-type display, a 40 nanometer-thick Ag film was deposited on ITO coated glass with the deposition rate of 0.1 nm/s. Then the atomic layer deposition of Al_2O_3 (30 cycles) was conducted to prevent the sputtering damage. WO_3 with the thickness of 100, 70 and 48 nm was deposited for red, green and blue device, respectively. Finally, 40 nanometer-thick Ag film was deposited again. Photolithography was conducted to reduce the area of transmissive type devices. After thorough rinsing with acetone and isopropanol, samples were dried by N_2 blowing followed by dehydration for 5 min on 150 °C hotplate. HMDS was spin-

coated (4000 rpm, 30 s) and baked for 3 min at 120 °C. AZ5214 photoresist was spin-coated at 4000 rpm for 30 s, and soft bake was conducted at 100 °C. After UV exposure (4 s, 15 mW/cm²) with MDA-400s mask aligner, developing was conducted by immersing the wafer into AZ300MIF developer for 40 s. Finally Ar ion beam milling was conducted for 1 min to partially remove the top Ag film.

Transmission type device shows additional novel functionality, light on/off switching, as well as color purifying. Due to the FP resonance on WO₃ sandwiched Ag layers, the light-WO₃ interaction is enhanced. Transmitted light almost turns off at the state 6 by intercalating Li⁺. Optical spectrum analysis was conducted with Cary 60 UV-VIS spectrometer (Cary, US). Simulation and experimental results show good agreement as shown in Figure 4.14.

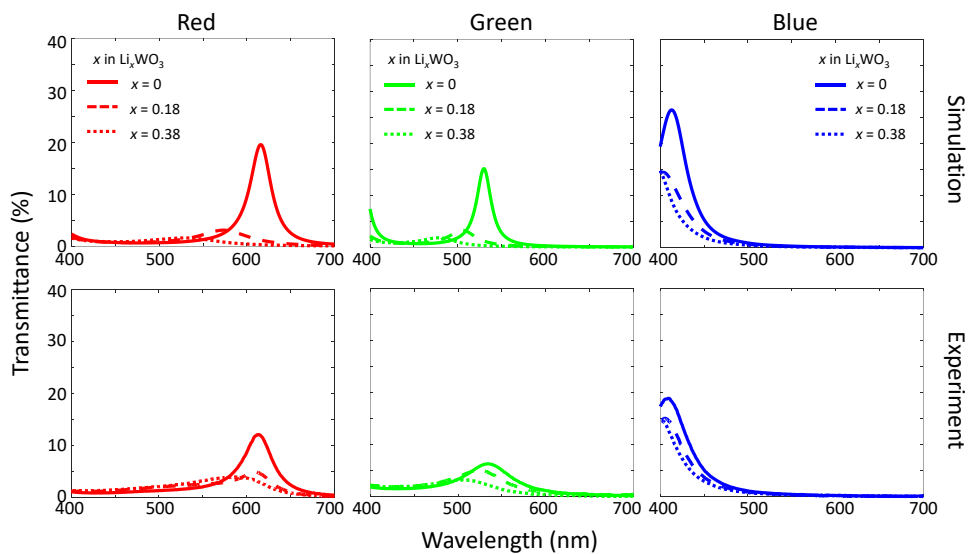


Figure 4.14. Spectra tuning of transmitted light for R, G, B. Light on/off corresponding to each same colored spectrum from state 1 through 4 to 6 (inset).

4.4 Conclusion

The nanometer-thick WO_3 was successfully incorporated to the electrochromic nano-optical device, showing wide and rich color expression and switching capability. The devices that solely depend on the light absorption of WO_3 film should employ thicker film to lengthen the light path. Therefore, conventional WO_3 -based films have the disadvantages of large power consumption and slow response time. On the other hand, in this thesis, the weak light modulation capability due to reduced thickness of WO_3 is overcome by the designed nanostructure with sophisticated material selection. The Si is generally considered as a poor reflector, however, WO_3 -on-Si system was able to represent rich color due to its moderate reflectance. The resonance wavelength blue shifted as Li^+ was intercalated into the WO_3 with reduced reflectance and turned back to the uncharged state reversibly. The transmissive device constructed with WO_3 thin film showed better color purity compared to the reflective type device due to its metal-insulator-metal structure which can trap light more efficiently. The Li intercalation turned off the device with a diminished-blue-shifted resonance in the intermediated states. The fast reversibility has not been achieved due to the dissolution of top Ag layer, however, it could be implemented by employing thin dielectric layer at Ag- WO_3 -Ag configuration. The full-colored smart window and electronic paper is expected to be developed by further optimization of these

conceptual devices.

Chapter 5. Conclusion

In this dissertation, electrically tunable optical devices based on oxide semiconductors, indium tin oxide and tungsten trioxide, are proposed. The amplitude, phase, and spectrum are dynamically controlled in visible and NIR regime. The ITO-and WO_3 -based nanostructures are carefully designed and numerically and experimentally demonstrated. Here, the summary of the results of this dissertation is presented as follows.

In Chapter 2, an ITO-based transmission modulator with electric bias was demonstrated. ITO, a kind of transparent conducting oxide, has intensively used as an electro-optic material to control optical input signals from IR to NIR region. Although most of previous studies on electrical tuning with based ITO have treated the reflected light, the transmittance is controlled with fast switching speed by applied bias in this dissertation. The proposed device is designed with a Si layer as a high index material added to the nanoscale MOS capacitor. This configuration can support two strong optical resonances, guided mode resonance and hybrid plasmonic waveguide resonance, providing enhanced the interaction between light and active region in ITO. To minimize leakage current breaking the insulator, the nano-patterns are fabricated to exist only in the restricted region with photolithography and e-beam lithography. This novel configuration has

many potential applications for ultracompact optical components, such as nanoscale spatial light modulator, tunable ultrathin lens, and dynamic holograms.

In Chapter 3, an electro-optic multifunctional metasurface at a fixed target wavelength is proposed. This ITO-based device with hyperbolic metamaterial substrate can simultaneously control the amplitude and phase of the reflected light. In case of normal incidence, the gap plasmon mode is formed between top metal layer and metallic nanograting. At this resonance, light is strongly confined so that the reflection is nearly zero, resulting in large phase shift with applied bias. The light cannot penetrate into substrate due to dielectric tensor of hyperbolic metamaterial. On the other hand, in case of oblique incidence, hyperbolic metamaterial substrate can support confined mode called bulk plasmon polaritons. The amplitude is modulated using the resonance coupling of gap plasmon polariton and bulk plasmon polariton formed inside HMM substrate. The proposed mechanism in optical mode engineering can open a new pathway to design practical multifunctional applications such as miniaturized multi-sensing systems and spatial light modulators capable of phase and amplitude modulation for the next generation ultracompact integrated optical systems.

In Chapter 4, electrically driven color-tunable devices are suggested and experimentally demonstrated. WO_3 as an electrochromic material is deposited on highly doped Si and the thickness of WO_3 thin film determines the visible spectrum of reflected light corresponding to a specific color. The

optical properties of WO_3 change by Li^+ intercalation, resulting in color tuning. Furthermore, for wide range of applications, the color-purified transmission type display device with simple film depositions is suggested. A centimeter-scale display is fabricated and color tuning and on/off switching are experimentally demonstrated. This research is expected to contribute greatly to the development of electronic papers, and the commercialization of novel low-powered full-color display in the near future.

Bibliography

1. H. Raether, *Surface Plasmons on Smooth and Rough Surfaces and on Gratings* (1988).
2. W. L. Barnes, A. Dereux, and T. W. Ebbesen, "Surface plasmon subwavelength optics.," *Nature* (2003).
3. D. K. Gramotnev and S. I. Bozhevolnyi, "Plasmonics beyond the diffraction limit," *Nat. Photonics* (2010).
4. E. Betzig and J. K. Trautman, "Near-field optics: Microscopy, spectroscopy, and surface modification beyond the diffraction limit," *Science* (80-.). (1992).
5. S. Kawata, Y. Inouye, and P. Verma, "Plasmonics for near-field nano-imaging and superlensing," *Nat. Photonics* (2009).
6. M. A. Noginov, G. Zhu, A. M. Belgrave, R. Bakker, V. M. Shalaev, E. E. Narimanov, S. Stout, E. Herz, T. Suteewong, and U. Wiesner, "Demonstration of a spaser-based nanolaser," *Nature* (2009).
7. Y. J. Lu, J. Kim, H. Y. Chen, C. Wu, N. Dabidian, C. E. Sanders, C. Y. Wang, M. Y. Lu, B. H. Li, X. Qiu, W. H. Chang, L. J. Chen, G. Shvets, C. K. Shih, and S. Gwo, "Plasmonic nanolaser using epitaxially grown silver film," *Science* (80-.). (2012).
8. A. V. Kabashin, P. Evans, S. Pastkovsky, W. Hendren, G. A. Wurtz, R. Atkinson, R. Pollard, V. A. Podolskiy, and A. V. Zayats, "Plasmonic nanorod metamaterials for biosensing," *Nat. Mater.* **8**(11), 867–871 (2009).
9. B. Luk'yanchuk, N. I. Zheludev, S. A. Maier, N. J. Halas, P. Nordlander, H. Giessen, and C. T. Chong, "The Fano resonance in plasmonic nanostructures and metamaterials.," *Nat. Mater.* **9**(9), 707–15 (2010).
10. D. Schurig, J. J. Mock, B. J. Justice, S. A. Cummer, J. B. Pendry, A. F. Starr, and D. R. Smith, "Metamaterial electromagnetic cloak at microwave frequencies," *Science* (80-.). (2006).
11. J. Valentine, S. Zhang, T. Zentgraf, E. Ulin-Avila, D. A. Genov, G. Bartal, and X. Zhang, "Three-dimensional optical metamaterial with a negative refractive index," *Nature* (2008).
12. N. Yu and F. Capasso, "Flat optics with designer metasurfaces.," *Nat. Mater.*

- (2014).
13. N. Engheta and R. W. Ziolkowski, *Metamaterials* (John Wiley & Sons, Inc., 2006).
 14. M. Khorasaninejad, W. T. Chen, R. C. Devlin, J. Oh, A. Y. Zhu, and F. Capasso, "Metalenses at visible wavelengths: Diffraction-limited focusing and subwavelength resolution imaging," *Science* (80-.). (2016).
 15. W. T. Chen, A. Y. Zhu, V. Sanjeev, M. Khorasaninejad, Z. Shi, E. Lee, and F. Capasso, "A broadband achromatic metalens for focusing and imaging in the visible.," *Nat. Nanotechnol.* (2018).
 16. M. S. Rill, S. Linden, J. K. Gansel, M. Thiel, M. Decker, K. Bade, G. von Freymann, V. Saile, and M. Wegener, "Gold Helix Photonic Metamaterial as Broadband Circular Polarizer," *Science* (80-.). **325**(5947), 1513–1515 (2009).
 17. Y. Zhao, M. A. Belkin, and A. Alù, "Twisted optical metamaterials for planarized ultrathin broadband circular polarizers," *Nat. Commun.* (2012).
 18. N. Yu, F. Aieta, P. Genevet, M. A. Kats, Z. Gaburro, and F. Capasso, "A broadband, background-free quarter-wave plate based on plasmonic metasurfaces," *Nano Lett.* (2012).
 19. X. Ni, A. V. Kildishev, and V. M. Shalaev, "Metasurface holograms for visible light," *Nat. Commun.* (2013).
 20. P. Genevet and F. Capasso, "Holographic optical metasurfaces: A review of current progress," *Reports Prog. Phys.* (2015).
 21. Y. Lee, S. J. Kim, H. Park, and B. Lee, "Metamaterials and metasurfaces for sensor applications," *Sensors (Switzerland)* (2017).
 22. K. V. Sreekanth, Y. Alapan, M. Elkabbash, E. Ilker, M. Hinczewski, U. A. Gurkan, A. De Luca, and G. Strangi, "Extreme sensitivity biosensing platform based on hyperbolic metamaterials," *Nat. Mater.* **15**(6), 621–627 (2016).
 23. N. Liu, M. Mesch, T. Weiss, M. Hentschel, and H. Giessen, "Infrared perfect absorber and its application as plasmonic sensor," *Nano Lett.* **10**(7), 2342–2348 (2010).
 24. Y. F. Yu, A. Y. Zhu, R. Paniagua-Domínguez, Y. H. Fu, B. Luk'yanchuk, and A. I. Kuznetsov, "High-transmission dielectric metasurface with 2π

- phase control at visible wavelengths," *Laser Photonics Rev.* (2015).
25. R. C. Devlin, A. Ambrosio, N. A. Rubin, J. P. Balthasar Mueller, and F. Capasso, "Arbitrary spin-to-orbital angular momentum conversion of light," *Science* (80-.). (2017).
 26. Z. Zhu, P. G. Evans, R. F. Haglund, and J. G. Valentine, "Dynamically Reconfigurable Metadevice Employing Nanostructured Phase-Change Materials," *Nano Lett.* **17**(8), 4881–4885 (2017).
 27. Y. W. Huang, H. W. H. Lee, R. Sokhoyan, R. A. Pala, K. Thyagarajan, S. Han, D. P. Tsai, and H. A. Atwater, "Gate-Tunable Conducting Oxide Metasurfaces," *Nano Lett.* **16**(9), 5319–5325 (2016).
 28. J. Park, J. H. Kang, S. J. Kim, X. Liu, and M. L. Brongersma, "Dynamic reflection phase and polarization control in metasurfaces," *Nano Lett.* **17**(1), 407–413 (2017).
 29. X. Duan, S. Kamin, and N. Liu, "Dynamic plasmonic colour display," *Nat. Commun.* **8**, 14606 (2017).
 30. X. Duan and N. Liu, "Scanning Plasmonic Color Display," *ACS Nano* **12**(8), 8817–8823 (2018).
 31. A. Tittl, P. Mai, R. Taubert, D. Dregely, N. Liu, and H. Giessen, "Palladium-based plasmonic perfect absorber in the visible wavelength range and its application to hydrogen sensing.," *Nano Lett.* **11**(10), 4366–9 (2011).
 32. P. Yu, J. Li, S. Zhang, Z. Jin, G. Schütz, C. W. Qiu, M. Hirscher, and N. Liu, "Dynamic Janus Metasurfaces in the Visible Spectral Region," *Nano Lett.* **18**(7), 4584–4589 (2018).
 33. Y. Chen, X. Duan, M. Matuschek, Y. Zhou, F. Neubrech, H. Duan, and N. Liu, "Dynamic Color Displays Using Stepwise Cavity Resonators," *Nano Lett.* **17**(9), 5555–5560 (2017).
 34. N. I. Zheludev and E. Plum, "Reconfigurable nanomechanical photonic metamaterials," *Nat. Nanotechnol.* (2016).
 35. Y. Yao, M. A. Kats, P. Genevet, N. Yu, Y. Song, J. Kong, and F. Capasso, "Broad electrical tuning of graphene-loaded plasmonic antennas," *Nano Lett.* (2013).
 36. N. Dabidian, I. Kholmanov, A. B. Khanikaev, K. Tatar, S. Trendafilov, S. H.

- Mousavi, C. Magnuson, R. S. Ruoff, and G. Shvets, "Electrical switching of infrared light using graphene integration with plasmonic Fano resonant metasurfaces," *ACS Photonics* (2015).
37. Y. C. Jun, J. Reno, T. Ribaldo, E. Shaner, J. J. Greffet, S. Vassant, F. Marquier, M. Sinclair, and I. Brener, "Epsilon-near-zero strong coupling in metamaterial-semiconductor hybrid structures," *Nano Lett.* (2013).
 38. P. Hosseini, C. D. Wright, and H. Bhaskaran, "An optoelectronic framework enabled by low-dimensional phase-change films," *Nature* (2014).
 39. S. J. Kim, H. Yun, K. Park, J. Hong, J. G. Yun, K. Lee, J. Kim, S. J. Jeong, S. E. Mun, J. Sung, Y. W. Lee, and B. Lee, "Active directional switching of surface plasmon polaritons using a phase transition material," *Sci. Rep.* (2017).
 40. S.-J. Kim, S. Choi, C. Choi, Y. Lee, J. Sung, H. Yun, J. Jeong, S.-E. Mun, Y. W. Lee, and B. Lee, "Broadband efficient modulation of light transmission with high contrast using reconfigurable VO₂ diffraction grating," *Opt. Express* (2018).
 41. Y. Liu, K. Tom, X. Wang, C. Huang, H. Yuan, H. Ding, C. Ko, J. Suh, L. Pan, K. A. Persson, and J. Yao, "Dynamic Control of Optical Response in Layered Metal Chalcogenide Nanoplates," *Nano Lett.* (2016).
 42. J. Park, J. H. Kang, X. Liu, and M. L. Brongersma, "Electrically Tunable Epsilon-Near-Zero (ENZ) Metafilm Absorbers," *Sci. Rep.* (2015).
 43. G. Kafaie Shirmanesh, R. Sokhoyan, R. A. Pala, and H. A. Atwater, "Dual-Gated Active Metasurface at 1550 nm with Wide (>300°) Phase Tunability," *Nano Lett.* **18**(5), 2957–2963 (2018).
 44. Y. Lee, S.-J. Kim, J.-G. Yun, C. Kim, S.-Y. Lee, and B. Lee, "Electrically tunable multifunctional metasurface for integrating phase and amplitude modulation based on hyperbolic metamaterial substrate," *Opt. Express* **26**(24), 32063 (2018).
 45. H. Wang, X. Wang, C. Yan, H. Zhao, J. Zhang, C. Santschi, and O. J. F. Martin, "Full Color Generation Using Silver Tandem Nanodisks," *ACS Nano* **11**(5), 4419–4427 (2017).
 46. L. Duempelmann, A. Luu-Dinh, B. Gallinet, and L. Novotny, "Four-Fold Color Filter Based on Plasmonic Phase Retarder," *ACS Photonics* **3**(2),

- 190–196 (2016).
47. C. S. Park, V. R. Shrestha, W. Yue, S. Gao, S. S. Lee, E. S. Kim, and D. Y. Choi, "Structural Color Filters Enabled by a Dielectric Metasurface Incorporating Hydrogenated Amorphous Silicon Nanodisks," *Sci. Rep.* **7**(1), 1–9 (2017).
 48. W. Yue, S. Gao, S. S. Lee, E. S. Kim, and D. Y. Choi, "Subtractive Color Filters Based on a Silicon-Aluminum Hybrid-Nanodisk Metasurface Enabling Enhanced Color Purity," *Sci. Rep.* **6**(June), 1–7 (2016).
 49. T. Ye, Y. Xiang, H. Ji, C. Hu, and G. Wu, "Electrodeposition-based electrochromic devices with reversible three-state optical transformation by using titanium dioxide nanoparticle modified FTO electrode," *RSC Adv.* **6**(37), 30769–30775 (2016).
 50. S. Araki, K. Nakamura, K. Kobayashi, A. Tsuboi, and N. Kobayashi, "Electrochemical optical-modulation device with reversible transformation between transparent, mirror, and black," *Adv. Mater.* **24**(23), 122–126 (2012).
 51. K. Xiong, D. Tordera, G. Emilsson, O. Olsson, U. Linderhed, M. P. Jonsson, and A. B. Dahlin, "Switchable Plasmonic Metasurfaces with High Chromaticity Containing Only Abundant Metals," *Nano Lett.* **17**(11), 7033–7039 (2017).
 52. K. Xiong, G. Emilsson, A. Maziz, X. Yang, L. Shao, E. W. H. Jager, and A. B. Dahlin, "Electronic Paper: Plasmonic Metasurfaces with Conjugated Polymers for Flexible Electronic Paper in Color (*Adv. Mater.* 45/2016)," *Adv. Mater.* **28**(45), 10103–10103 (2016).
 53. F. Sterl, N. Strohfeldt, R. Walter, R. Griessen, A. Tittl, and H. Giessen, "Magnesium as Novel Material for Active Plasmonics in the Visible Wavelength Range," *Nano Lett.* **15**(12), 7949–7955 (2015).
 54. A. L. Holsteen, S. Raza, P. Fan, P. G. Kik, and M. L. Brongersma, "Purcell effect for active tuning of light scattering from semiconductor optical antennas," *Science* (80-.). (2017).
 55. E. Feigenbaum, K. Diest, and H. A. Atwater, "Unity-order index change in transparent conducting oxides at visible frequencies," *Nano Lett.* **10**(6), 2111–2116 (2010).

56. X. Liu, J.-H. Kang, H. Yuan, J. Park, Y. Cui, H. Y. Hwang, and M. L. Brongersma, "Tuning of Plasmons in Transparent Conductive Oxides by Carrier Accumulation," *ACS Photonics* **5**(4), 1493–1498 (2018).
57. M. Z. Alam, I. De Leon, and R. W. Boyd, "Large optical nonlinearity of indium tin oxide in its epsilon-near-zero region," *Science* (80-.). **352**(6287), 795–797 (2016).
58. J. M. Jaksic, D. Labou, G. D. Papakonstantinou, A. Siokou, and M. M. Jaksic, "Novel spillover interrelating reversible electrocatalysts for oxygen and hydrogen electrode reactions," *J. Phys. Chem. C* **114**(43), 18298–18312 (2010).
59. M. Akiyama, J. Tamaki, N. Miura, and N. Yamazoe, " Tungsten Oxide-Based Semiconductor Sensor Highly Sensitive to NO and NO₂ ," *Chem. Lett.* (2006).
60. G. Gu, B. Zheng, W. Q. Han, S. Roth, and J. Liu, "Tungsten Oxide Nanowires on Tungsten Substrates," *Nano Lett.* (2002).
61. V. R. Buch, A. K. Chawla, and S. K. Rawal, "Review on electrochromic property for WO₃ thin films using different deposition techniques," in *Materials Today: Proceedings* (2016).
62. R. F. Oulton, V. J. Sorger, D. A. Genov, D. F. P. Pile, and X. Zhang, "A hybrid plasmonic waveguide for subwavelength confinement and long-range propagation," *Nat. Photonics* **2**(8), 496–500 (2008).
63. I. Avrutsky, I. Salakhutdinov, J. Elser, and V. Podolskiy, "Highly confined optical modes in nanoscale metal-dielectric multilayers," 2–5 (2007).
64. G. A. Niklasson, C. G. Granqvist, and O. Hunderi, "Effective medium models for the optical properties of inhomogeneous materials," *Appl. Opt.* (2008).
65. S. V. Zhukovsky, O. Kidwai, and J. E. Sipe, "Physical nature of volume plasmon polaritons in hyperbolic metamaterials," *Opt. Express* (2013).
66. K. Hwi, P. Junghyun, and L. Byounggho, *Fourier Modal Method and Its Applications in Computational Nanophotonics* (CRC Press, 2017).
67. W. Weppner, "Determination of the Kinetic Parameters of Mixed-Conducting Electrodes and Application to the System Li₃Sb," *J. Electrochem. Soc.* **124**(10), 1569 (1977).

68. R. Ji, D. Zheng, C. Zhou, J. Cheng, J. Yu, and L. Li, "Low-temperature preparation of tungsten oxide anode buffer layer via ultrasonic spray pyrolysis method for large-area organic solar cells," *Materials (Basel)*. (2017).

Appendix

Some portions of the work in this dissertation are also presented in the following publications:

Chapter 3:

Y. Lee, S.-J. Kim, J.-G. Yun, C. Kim, S.-Y. Lee, and B. Lee, "Electrically tunable multifunctional metasurface for integrating phase and amplitude modulation based on hyperbolic metamaterial substrate," *Optics Express*, vol 26, no. 24, pp. 32063-32073, 2018.

초 록

지난 10 년간, 초소형 광전자 변조기 및 재구성이 가능한 메타 표면과 같은 능동 제어 나노 광소자 장치를 구현하는데 많은 노력이 기울여졌다. 근적외선 (NIR) 및 가시 광선 대역에서, 능동 물질과 나노 구조를 결합한 형태로 기계적 구동, 화학적 활성화, 전하 주입 등을 포함한 다양한 메커니즘이 제안되었다. 특히 전기적 제어는 저전력 소비, 빠른 스위칭 속도 및 기존 전자 장치와의 호환성과 같은 뚜렷한 이점을 제공하는 측면에서 가장 유망한 기술 중 하나로 평가받고 있다.

이 학위 논문에서는, 위상, 진폭 및 스펙트럼과 같은 빛의 일반적인 특성을 근적외선 및 가시광 영역에서 인가전압을 통해 제어하는 내용을 다룬다. 우선, NIR 범위의 광 신호를 전기적으로 제어하기 위해, 대표적인 투명 전도성 산화물인 인듐 주석 산화물을 기반으로 하는 진폭 변조기가 제안되었다. 기존에 주로 연구되었던 금속-절연체-금속 기반 반사형 변조 시스템은 입사광과 반사광을 서로 분리하기 위해 빔 분할기 및 편광기와 같은 추가 광학 요소를 필요로 하는 어려움이 있다. 이에 반사형 구조를 벗어나, 나노 스케일 인듐 주석 산화물 기반 축전기와 굴절률 물질인 실리콘 층을 사용한 투과형 진폭 변조기가 제안되었다. 이 변조기는 하이브리드 플라즈몬 도파로 모드와 순수 도파로 모드의 두 가지 유형의 강한 광학적 공진을 기반으로 작동하도록 설계되었다. 이러한 모드는 보다 강한 빛과 능동 물질의 상호작용을 가능하게 하여, 물질의 굴절률 변화를 민감하게 감지할 수 있게 한다.

둘째, 하나의 고정된 파장에서 두 가지 기능을 구현하도록 설계된 전기적 구동 기반 메타 표면이 제안되었다. 인듐 주석

산화물 집적 구조 기반의 본 장치는 입사광의 상태에 따라 반사광의 위상 또는 진폭을 변조 할 수 있다. 수직 입사의 경우, 위상 변조는 인듐 주석 산화물 층에 강하게 형성된 갭 플라즈몬 모드를 통해 이루어진다. 또한, 동일한 구조적 기초 위에서 다른 기능을 수행하기 위해, 쌍곡선 메타 물질 기판을 적용함으로써 또 다른 유형의 모드가 이용 될 수 있다. 사입사의 경우, 진폭 변조는 이러한 벌크 플라즈몬 모드를 사용함으로써 구현된다.

이 학위 논문의 마지막 부분은 가시광 영역의 스펙트럼을 전기적으로 변조하는 내용을 담고 있다. 광범위하게 사용되고 있는 전기 변색 물질인 텅스텐 산화물을 기반으로 하여, 전기적으로 색을 제어할 수 있는 소자를 제작하였다. 제안된 소자는 까다로운 공정 기법을 필요로 하지 않는 간단한 구조로서 다양한 색상 생성 및 고 대비 색상 튜닝이 가능하다.

이 논문은 가까운 장래에 새로운 저전력 풀 컬러 디스플레이의 상용화와 집적 광학 회로의 구현에 기여할 것으로 기대된다.

주요어 : 전기적 제어, 인듐 주석 산화물, 텅스텐 산화물, 광공진
학 번 : 2014-21682